



Taguchi-based experimental investigation into weld cladding of Ni-WC MMC overlays by CMT process

Mohammad Reza Karimi¹ · Sheng-Hui Wang² · Jasmin Jelovica^{1,3}

Received: 14 April 2022 / Accepted: 18 July 2022 / Published online: 3 September 2022
© Crown 2022

Abstract

In the search for versatile and effective weld cladding processes to deposit ultra-wear-resistant Ni-WC MMC (Ni-based tungsten carbide metal matrix composite) overlays for mining applications, there is an increasing interest in exploring advanced low-heat-input cold metal transfer (CMT) method. Depositions of single weld bead tracks of Ni-WC MMCs on steel plates were performed by employing the CMT process; Taguchi's design of experiments was used to plan the experimental investigation. All weld tracks exhibit continuous and uniform bead profile and sound metallurgical bonding to the substrate. Retained WCs are present in the overlay tracks relatively uniformly. The formation of primary WC and secondary carbides is observed depending on the level of dilution. In contrast to standard gas metal arc welding processes, the volume fraction of retained WC, which is negatively correlated with dilution level, is not directly interrelated with heat input for the CMT process and can reach a high level together with improved weld bead appearance at high deposition rate. Deposition rate has a positive correlation with average instantaneous power, which is, in turn, positively correlated with wire feed speed. The addition of oxygen into shielding gas mixtures promotes carbide transfer from cored feed wire to the weld track and increases the volume fraction of retained WC. Analysis of signal-to-noise ratios shows that it is difficult to find a single set of optimized processing parameters, and trade-offs are needed in engineering practice. The present investigation demonstrates that the Taguchi method is a powerful tool in process improvement for weld cladding of Ni-WC MMC overlays.

Keywords Weld cladding · Cold metal transfer (CMT) · Carbide transfer efficiency · Retained WC · Carbide dissolution · Taguchi design of experiments

Abbreviations

η	Carbide transfer efficiency	A_R	Reinforcement area of a weld bead
θ	Contact angle of a weld bead	A_{WC}	Total cross-sectional area of WC particles
ρ_p	Density of powders (wrapped within nickel sheath)	BSE	Backscattered electrons
AIP	Average instantaneous power	CMT	Cold metal transfer
$A_{Ni-sheath}$	Nickel sheath area	DL	Dilution level
A_p	Area of weld penetration	DOE	Design of experiments
		DR	Deposition rate
		EDS	Energy-dispersive X-ray spectrometer
		f_p	Initial volume fraction of carbide particles in cored feed wire
		f_{WC}	Volume fraction of retained WC
		GMAW	Gas metal arc welding
		H	Height of weld bead
		HI	Heat input
		I	Current
		l_m	Linear mass of the electrode
		Ni-WC MMC	Nickel-based metal matrix composites reinforced with WC
		P	Penetration depth

✉ Sheng-Hui Wang
sheng-hui.wang@nrc-cnrc.gc.ca

¹ Department of Mechanical Engineering, The University of British Columbia, 6250 Applied Science Lane, Vancouver, BC V6T 1Z4, Canada

² Energy, Mining and Environment Research Centre, National Research Council of Canada, 4250 Wesbrook Mall, Vancouver, BC V6T 1W5, Canada

³ Department of Civil Engineering, The University of British Columbia, 6250 Applied Science Lane, Vancouver, BC V6T 1Z4, Canada

P_p	Powder weight percentage
S/N ratio	Signal-to-noise ratio
SEM	Scanning electron microscopy
SG	Shielding gas
TS	Travel speed
V	Voltage
W	Width of a weld bead
W/H	Width to height ratio of a weld bead
WC	Mono-crystalline tungsten carbide
WFS	Wire feed speed
XRD	X-ray diffraction

1 Introduction

For hard-rock and oil-sands mining operations, machinery and structural components are often subjected to extremely harsh operational conditions and experience significant material losses, leading to increased equipment downtime [1]. For instance, damage caused by the wear of equipment and machinery in mining (including mining of oil-sands) and gas sectors in Canada was approximately C\$2.5 billion/year in the 1980s [2]. In 2003, it was reported that this amount was over C\$450 million for repair and maintenance of equipment at the main oil-sand-mining operators [3]. Thick protective overlays are increasingly used to protect machinery and equipment from damage under these harsh conditions. These typically come in the form of chromium carbide-based overlays (CCOs) and nickel-based metal matrix composites reinforced with WC (Ni-WC MMCs). These overlays can extend the service life of production-critical components, reducing costs related to maintenance, repair, and operations [4]. The material system of Ni-WC MMC is fundamentally different from CCOs in the way that WC is not formed in situ (through nucleation and growth) during the solidification process; instead, WC particles are incorporated in the feed materials and should remain unmelted during welding deposition [5]. Moreover, Ni-WC MMCs have higher wear resistance in comparison to CCOs and are used in applications where components work in more severe corrosive and erosive environments. The superior wear resistance of Ni-WC MMC overlays lies mainly in the existence of the retained hard WC particles in the overlays [6]. However, preferential dissolution of the WC particles incorporated in the feed material has been reported during the deposition of Ni-WC MMCs [7, 8]. The excessive dissolution of these particles significantly reduces the amount of retained hard WC carbides in the overlays and can lead to the formation of smaller and brittle W-rich carbides in the matrix during solidification [9], which adversely affects the wear resistance of the overlay [5]. In general, the degree of WC dissolution is inversely proportional to the level of heat input (HI) [10,

11]; therefore, deposition techniques featuring lower HI are sought for Ni-WC MMCs.

Welding-based processes that are employed to deposit Ni-WC MMC are laser cladding [12], plasma transferred arc welding (PTAW) [13], gas tungsten arc welding (GTAW) [14], and gas metal arc welding (GMAW) [15]. WC dissolution is reported for all of these processes. Laser cladding and PTAW processes could potentially deposit high-quality Ni-WC MMC overlays due to their low HI ; however, some related limitations make their applications for onsite repairs problematic or implausible. For instance, powder-based PTAW and laser cladding processes may only be utilized for the cases of flat welding positions; besides, they are susceptible to wind dispersion and not suited for large-size components, and have high capital and operating costs [16]. On the other hand, GMAW as a wire electrode-based process is a versatile and comparatively cheaper method, applicable for all welding positions, has a high deposition rate (DR) and requiring smaller-size power supplies. Nevertheless, high WC dissolution is reported for the GMAW process [5] due to the high HI .

For the GMAW cladding process, the relationship between WC dissolution and welding parameters (including HI) and other related factors (such as protection gases and substrate chemistry) is complicated. Choi et al. [4] achieved a high WC volume fraction while employing minimum HI to deposit Ni-WC MMC overlays by GMAW process, which led to less than 1% dilution, insufficient for oil-sand mining where high impact loading is often present. Badisch and Kirchgaßner [17] and Choi et al. [4] reported that dissolution of WC occurs during the GMAW process, regardless of whether the overlay was deposited over a steel plate or previously deposited Ni-WC MMC overlays. Vespa et al. [18] and Badisch and Kirchgaßner [17] determined that increasing wire feed speed (WFS) and welding voltage results in an increasing dilution and decreasing carbide volume fraction in the Ni-WC MMC overlays. Günther and Bergmann [19] observed that welding travel speed (TS) has no significant effect on the dilution for the studied parameters ranges. WC dissolution can occur during the droplet transfer and within the molten weld pool. As a result, to achieve a high-quality Ni-WC MMC overlay, HI must be kept to a minimum to limit the WC dissolution while maximizing their transfer efficiency [20]. However, adjusting the welding parameters to achieve the minimum droplet temperature does not guarantee the mitigation of WC dissolution. Scott [21] utilized welding parameters that led to the lowest HI but still observed partial dissolution of WC with poor weld bead appearance despite improved volume fraction of retained WC (f_{WC}). Guest [20] compared the effects of different shielding gas (SG) mixtures for depositing Ni-WC MMC and reported a significant increase in carbide transfer

Table 1 Chemical composition of ASTM A36 steel [34]

[wt.%]	C	P	S	Si	Cu	Fe
ASTM A36	0.26	0.04	0.05	0.4	0.20	Bal

efficiency (η) for Ar + O₂ in comparison to Ar + CO₂, showing a beneficial effect on O₂.

Besides the metallurgical dissolution of WC as discussed above, Guest [20, 22] also documented the non-wetting behavior of WC, resulting in a portion of WC particles not being caught up in the molten pool during the welding process, leading to low f_{WC} in Ni-WC MMC overlays due to mechanical loss of WC particles. This phenomenon was also reported by Günther et al. [23].

Weld cladding is a multi-factor, multi-response process. A substantial amount of time and cost is required to determine the optimal welding envelope by integrating different welding control parameters through trial and error [24]. Design of experiments (DOE) is one of the various methods to correlate input factors with responses [25]. Taguchi design is a widely accepted DOE method that utilizes orthogonal arrays to reduce the number of experiments.

Cold metal transfer (CMT) is a relatively new advancement of the GMAW process, enabling welding operations with reduced HI . CMT process is equipped with a highly precise waveform control system and a fast mechanically retracting wire feeding system that allows detachment of one droplet at a time and significantly reduces HI , distortion, and spatter [26]. CMT process has been utilized for various applications in industry, such as welding dissimilar materials [27], joining thin sheet metal [28], aluminum welding [29], and hardfacing [30]. With the CMT process, researchers achieved a low dilution level (DL) with a high DR for a set of experiments with low HI [31], mitigating the formation of the unwanted intermetallic layer in aluminum/steel welding [32]. It should be mentioned that the control of welding parameters of the CMT process involves a synergistic effect and is much more sophisticated compared to standard GMAW processes. According to Ola and Doern [33], while maintaining other parameters constant during depositing Ni-based INCONEL 718 superalloy overlay by the CMT process, HI is linearly related to WFS , which affects dilution and weld bead geometry; the contact angle (θ) was found to be significant in generating defect-free clad surfaces.

Considering the significance of HI in relation to WC dissolution, there is a strong interest in the deposition of Ni-WC MMC overlays by the CMT process. To the best

of the authors' knowledge, no articles have been published yet on depositing Ni-WC MMC overlays using tubular cored feed wire by this low- HI process. Therefore, it is necessary to perform experimental explorations to have a comprehensive understanding of the technological characteristics of weld cladding of resulting overlays by the CMT process: on the one hand, due to its uniqueness as compared to the standard GMAW processes, it is not clear how well the knowledge gained previously on welding cladding of Ni-WC MMC overlays by standard GMAW processes can be transferred to the case with CMT; on the other hand, due to the complex nature of weld cladding of related overlays as discussed above, it is crucial to find a suitable operating envelope to assure Ni-WC MMC overlay quality, such as minimizing the dissolution of the WC in the overlay without sacrificing other quality criteria if CMT process is engaged. While overall investigations are ongoing to compare CMT technology with standard GMAW in relation to the weld cladding processes, this paper reports processing development efforts to achieve high-quality Ni-WC MMC overlays by CMT process; single-bead Ni-WC MMC overlays were deposited for the investigation, and Taguchi design of experiments was used to systematically investigate the effect of welding parameters under CMT synergic mode on WC dissolution, η , DL , DR , and weld bead geometry.

2 Methodology

2.1 Materials and consumables

ASTM A36 hot rolled flat bar steel [34] is used as a substrate with the size of 100 mm × 75 mm × 10 mm. The surface of the substrate is ground, degreased, and cleaned with acetone prior to the welding. The feed material is a tubular Ni-based metal cored wire with a diameter of 1.6 mm and with WC particles incorporated in the core [35]. The chemical composition and specification of the substrate and the tubular cored feed wire are listed in Tables 1 and 2, respectively.

Table 2 Tubular cored wire specification [35]

Electrode commercial name	Supplier	Nominal composition	Nominal hardness
COR®FACE 164 MC	COR-MET	NiCrBSi-55 wt.% WC	Matrix = 38–42 HRC WC = 2600 Knoop

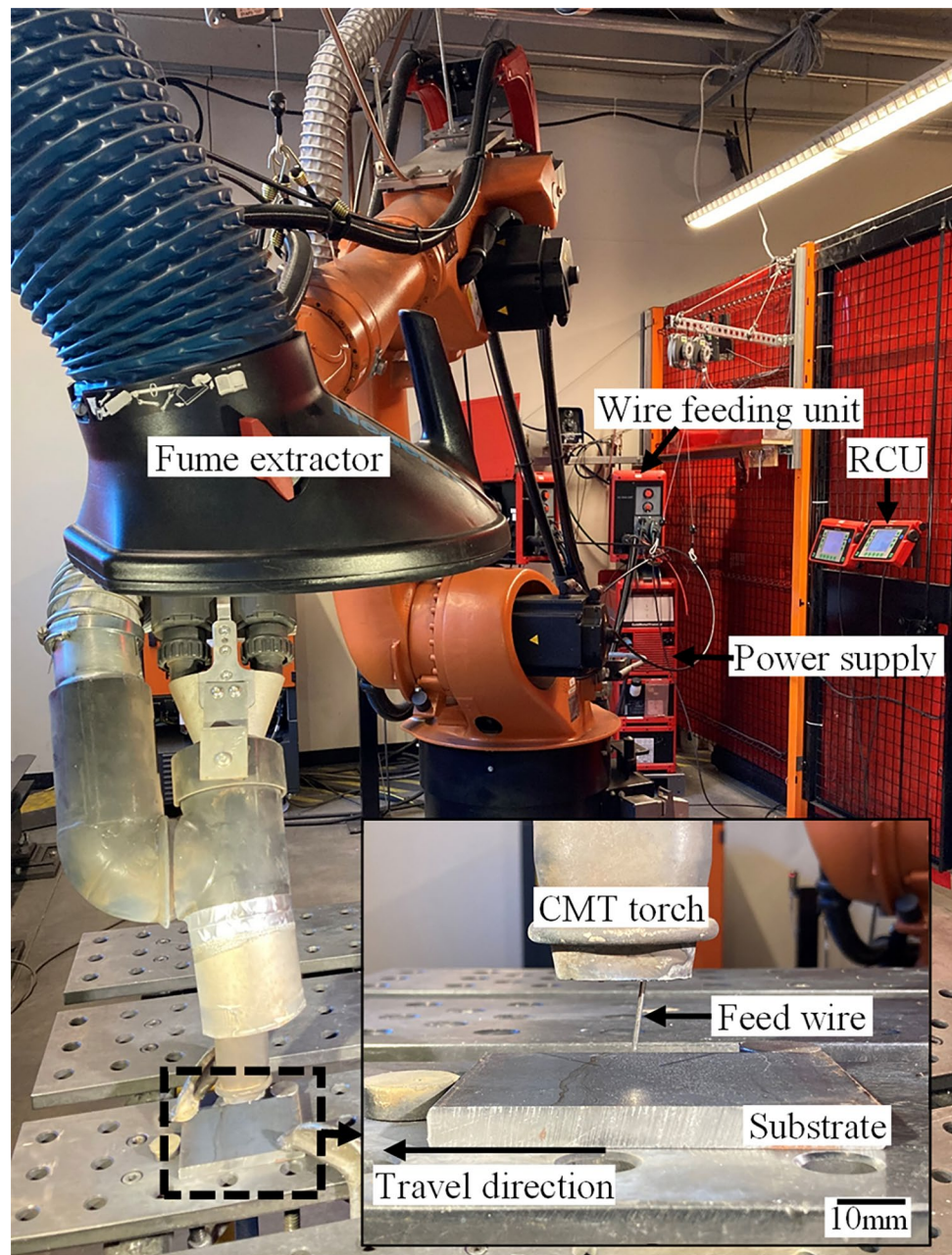
2.2 Experimental setup and design

As shown in Fig. 1, the welding system includes a Fronius TransPuls Synergic 5000 power supply with a RCU 5000i remote control unit and Fronius VR 7000 CMT wire feeding unit. The deposition process is carried out using a 6-axis KUKA robot KR 60 HA and KR C4 control system with a welding torch (Robacta Twin Compact Pro torch neck) mounted on its tool flange. This allows for fully automatic control of the welding process. Real-time welding current and arc voltage are measured at a sample rate of 20 kHz. The welding torch was positioned perpendicular to the substrate, which allowed a continuous supply of the feed wire during

welding deposition while keeping the angle between the wire and the substrate at 82° . Contact tip to work distance was kept at 15 mm for all experiments.

Based on the previous in-house knowledge of depositing Ni-WC MMC at the National Research Council of Canada (NRC)-Vancouver, the CMT synergic mode (CrNi19 12 cladding, ref. 1633) is set for conducting the experiments. The synergic mode is a pre-programmed operation mode. Once the electrode type/diameter, welding process mode, *WFS*, and *SG* mixture are selected, the welding power supply automatically adjusts the current and voltage. Moreover, *WFS* in this paper refers to a preset (nominal) value. As mechanically retracting of the feed wire occurs repetitively

Fig. 1 Snapshot of CMT welding machine and KUKA robot at NRC-Vancouver



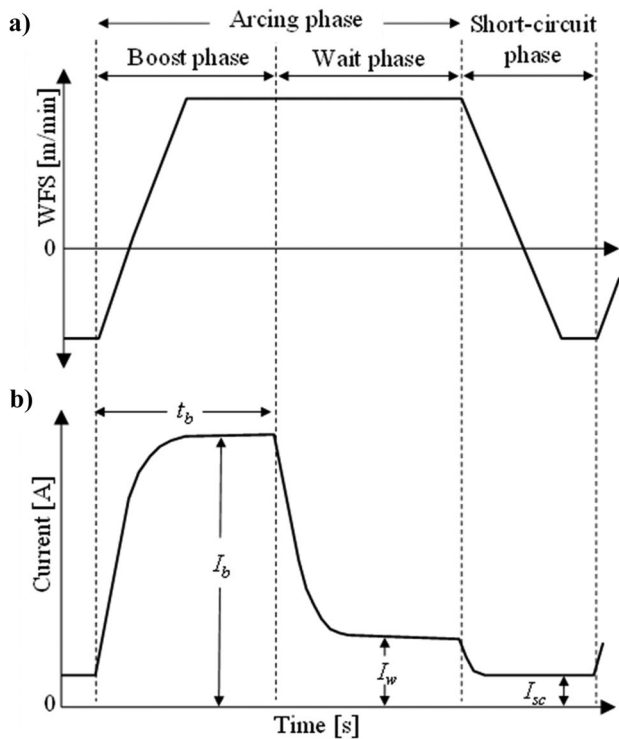


Fig. 2 Typical CMT waveform cycle: **a** *WFS* vs time (negative value corresponding to electrode retracting); **b** current vs time (I_b : boost current; t_b : boost duration; I_w : wait current; I_{sc} : short-circuit current)

(as indicated in Fig. 2a), the actual *WFS* can vary from the preset *WFS* in the CMT process [36].

The typical CMT waveform cycle is illustrated in Fig. 2. Characteristics of the cycle are listed in Table 3. The CMT cycle is defined as the period required to form and transfer a molten droplet into the weld pool, and it consists of two fundamental phases: short-circuiting and arcing phase. Arcing phase includes boost and wait phase. At the beginning of the boost phase, the current rapidly rises to the preset value (as indicated in Fig. 2b), reigniting the arc between electrode and substrate, and leading to the formation of a droplet at the tip of the electrode. Then, the electrode advances toward the weld pool while the current decreases to avoid globular transfer of the molten droplet; the voltage changes synergistically with the current. Once the molten droplet touches

the weld pool (beginning of the short-circuit phase), the current immediately drops near zero, and the electrode retracts, allowing the detachment and transfer of the molten droplet into the weld pool [37]. Duration of short-circuit phase is nonadjustable, once a CMT synergic mode is selected [36].

Taguchi DOE L16 orthogonal array is used for the systematic evaluation of the welding control parameters. The experiments are focused on the effect of the *WFS*, *TS*, and *SG* mixture (each at 4 levels) while keeping the other variables constant. The available range of *WFS* for the CMT synergic mode (CrNi19 12 cladding, ref. 1633) is 2.1–7.5 m/min. Accordingly, 2.1, 3.9, 5.7, and 7.5 m/min is selected as the four levels of *WFS*. It should be noted that a selection of *WFS* outside of the available synergic mode range necessitates creating a user-defined characteristic, which is beyond the scope of this study. The breakdown of the preset welding current waveform characteristics for each of the chosen *WFS* is listed in Table 3; the voltage will vary accordingly. As indicated in Fig. 2b and Table 3, the current level and its features differ significantly within one waveform cycle from one phase to another.

For standard GMAW, *TS* is one of the three factors in arc welding that affects the *HI*, along with current and voltage. *TS* range should ensure a defect-free deposition without sacrificing *DR*. In this paper, *TS* is set to 0.3–0.6 m/min with 0.1 increments. Four *SG* mixtures are selected for the study: 25% CO₂, 15% CO₂, 2% O₂, and 5% O₂ (Ar balanced). For *SG* mixtures, commercially available Praxair’s Ar–O₂ StarGold blend, CO₂, and Ar gas cylinder were used. Table 4 lists the welding control parameters and their levels used to deposit 16 different bead-on-plate experiments using the CMT process for a length of 50 mm. All experiments were successfully deposited with no discontinuity in the weld bead or any visual defect. In addition to Taguchi L16 experiments, two confirmation tests were conducted to validate optimum processing conditions predicted by the Taguchi design (see Sections 3.4 and 3.5 for details).

2.3 Characterization of the overlays

One of the critical features governing all welding processes is *HI*, which is often associated with the mechanical properties of the resultant overlay [20]. *HI* is a relative

Table 3 Preset waveform values for chosen *WFS*

Symbol	Unit	Definition	Synergic <i>WFS</i> guideline [m/min]			
			2.1	3.9	5.7	7.5
I_w	[A]	Current setpoint for wait phase, until the molten droplet touches the weld pool	35	60	82	110
I_{sc}	[A]	Current setpoint in the short-circuit phase	35	40	73	110
I_b	[A]	Current setpoint in the boost phase	225	290	307	340
t_b	[ms]	Maximum duration of the boost phase	3	3.75	5.13	5.6

Table 4 Taguchi L16 factors and levels

Std. order	WFS (m/min)	TS (m/min)	SG (%, Ar balanced)
1	2.1	0.3	25% CO ₂
2	2.1	0.4	15% CO ₂
3	2.1	0.5	2% O ₂
4	2.1	0.6	5% O ₂
5	3.9	0.3	15% CO ₂
6	3.9	0.4	25% CO ₂
7	3.9	0.5	5% O ₂
8	3.9	0.6	2% O ₂
9	5.7	0.3	2% O ₂
10	5.7	0.4	5% O ₂
11	5.7	0.5	25% CO ₂
12	5.7	0.6	15% CO ₂
13	7.5	0.3	5% O ₂
14	7.5	0.4	2% O ₂
15	7.5	0.5	15% CO ₂
16	7.5	0.6	25% CO ₂

measure of the energy transferred per unit length of a weld. For pulsed GMAW or CMT processes with complex waveforms, the traditional method of calculating HI (using average current and voltage) may not give the same result as using instantaneous values [38, 39]. Therefore, to accurately capture the changes in welding waveforms, the real-time current and voltage data were acquired at 20 kHz. Average instantaneous power (AIP) and HI are then calculated using Eqs. (1) and (2), respectively.

$$AIP [W] = \text{Total instantaneous power}/n = \sum_0^i(I_i \times V_i)/n \quad (1)$$

$$HI \left[\frac{kJ}{mm} \right] = \sum_0^i(I_i \times V_i) \times \Delta t / (t \times TS) \quad (2)$$

where I_i is the welding current, V_i is welding voltage for each sample, n is the number of samples, Δt is the sampling interval, and t is welding time. According to Joseph et al. [39], Eq. (1) is a simplified form of AIP calculation by using discretized voltage and current samples. It should be noted that the waveform characteristics of the voltage and current vary with changing WFS for a selected synergic mode, and therefore so does the HI . It is believed that process efficiency is higher for CMT as compared to standard GMAW [39–41]. As no agreed-upon efficiency factor is yet reported for the CMT process, for simplicity it is assumed that HI takes the value of the arc energy. As the efficiency factor should be similar for all samples, the assumption made here should not affect the overall discussions on the subject matter.

DR is defined as the actual weight of material deposited per unit of time. The plate was weighed three times with

0.001 g precision before and after the deposition of each single weld bead track, and the average values were used in Eq. (3) to calculate the DR .

$$DR \left[\frac{kg}{h} \right] = \frac{\text{Final weight} - \text{initial weight}}{t} \quad (3)$$

To investigate the microstructure and quality of the overlays, resultant samples were cut from three locations (first quarter, middle, and the third quarter of the weld bead track), hot mounted, ground, and polished. To reveal the fusion lines, samples were etched by 2% Nital. The cross-section was first locally photographed, and then a high-resolution image of the entire cross-section of the weld bead track at $\times 200$ magnification was constructed using the auto-stitch feature of the Keyence VHX-7000 series digital microscope. The resultant images were used to calculate the DL , f_{WC} , weld bead geometry, and porosity. The microstructures of tubular cored wire and the single-bead Ni-WC MMC overlays were investigated using scanning electron microscopy (SEM, HITACHI S-3500 N). Energy-dispersive X-ray spectrometer (EDS) capable of quantitative analysis and X-ray mapping was used to determine the composition of various phases in the samples.

The initial carbide volume fraction (f_p) of cored feed wire is considered the theoretical maximum of retained carbides that can be attained in the resultant overlays. This value is required to calculate η and monitor the carbide loss (due to WC dissolution or non-wetting behavior). f_p is a function of the linear mass of the electrode (l_m), powder weight percentage (P_p), density of powder (ρ_p), and nickel sheath area ($A_{Ni\text{-sheath}}$), which can be calculated using Eqs. (4)–(6) [42].

$$l_m = \frac{\text{Weight of electrode}}{\text{Length of electrode}} \quad (4)$$

$$P_p = \frac{\text{Weight of powder inside electrode}}{\text{Weight of electrode}} \quad (5)$$

$$f_p = \frac{(P_p \times l_m)}{(P_p \times l_m) + (A_{Ni\text{-sheath}} \times \rho_p)} \times 100\% \quad (6)$$

In order to find f_p , five samples of about 100 mm in length were cut from the electrode and weighted with 0.001 g precision to find the weights of the electrode, Ni-sheath, and the powder. All measurements are repeated three times, and the average value is reported. $A_{Ni\text{-sheath}}$ was measured by converting the cross-section image of the electrode (Fig. 3a) to the binary image (Fig. 3b) to facilitate measuring the Ni-sheath area in ImageJ software. Table 5 summarizes the measured values used to calculate the f_p .

The analysis shows that $l_m = 0.0170$ g/mm, $P_p = 54.58\%$ (which is similar to manufacturer's specification of 55 wt.%)

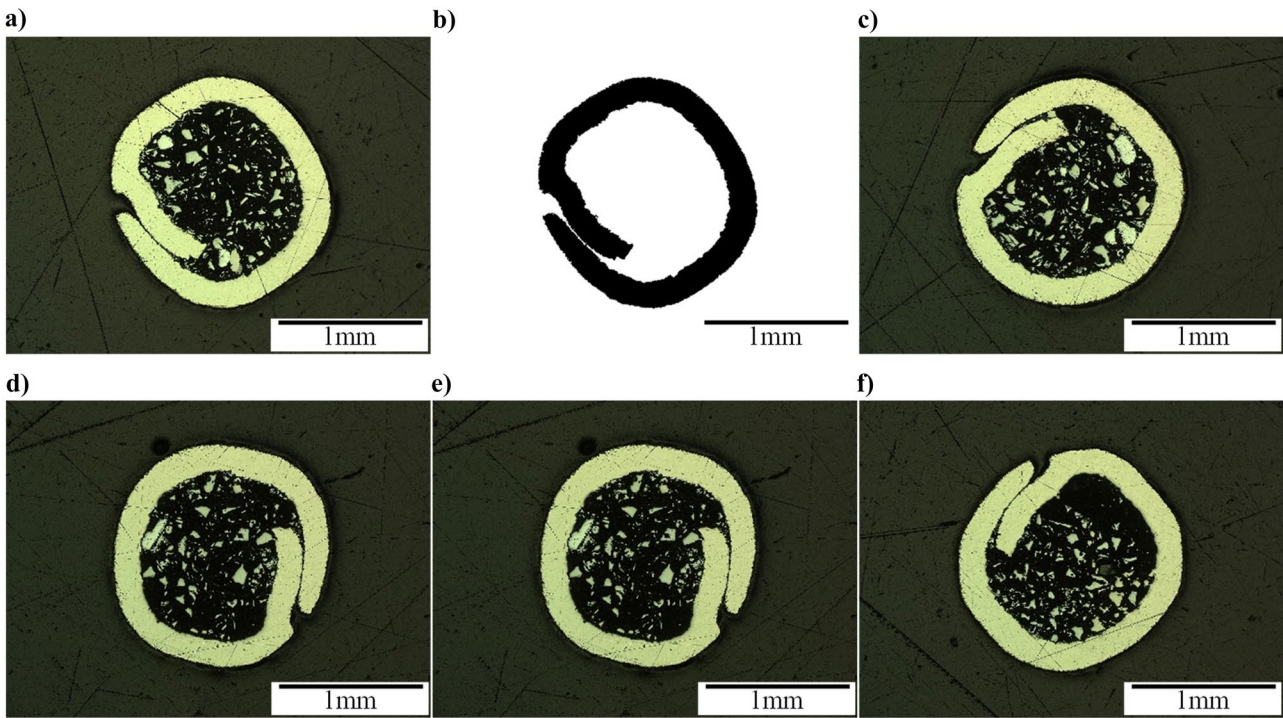


Fig. 3 Optical microscope image of tubular Ni-WC cored wire cross-section; **a** original image of sample 1; **b** binary image of sample 1; **c–f** original images of samples 2–5

[35] as listed in Table 2), $\rho_p = 16.67 \text{ g/cm}^3$ (assuming that the powder consists of only WC) and $A_{\text{Ni-sheath}} = 0.819 \text{ mm}^2$. Using these values in Eqs. (4)–(6), f_p is 40.4%.

Weld bead geometry measurement is conducted over the three prepared sample cross-sections for each experiment, and the average value is reported. Figure 4a illustrates the width (W), height (H), penetration depth (P), and contact angle ($\theta = \frac{\theta_1 + \theta_2}{2}$).

f_{WC} is calculated using Eq. (7). It is calculated as the ratio of A_{WC} (retained and primary WC area, see Fig. 4c) to the total overlay area ($A_R + A_P$, see Fig. 4d). Furthermore, η is an important measure of the effectiveness of related weld cladding process. η is the fraction of WC in feed wire, which is transferred to the overlay. A small portion of carbides transferred to the overlay will be dissolved, forming primary and secondary carbides during the solidification process; in theory, retained, primary, and secondary WC should all be measured to determine η . However, for simplicity, η is

calculated using Eq. (8), by taking into account only retained and primary WC while ignoring the secondary WC (as the latter consists of only a small fraction of the total transferred carbides and is difficult to quantify). In other words, η measures the amount of retained and primary WC in the overlay relative to the maximum achievable value (i.e., f_p).

$$f_{\text{WC}} (\%) = A_{\text{WC}} / (A_R + A_P) \tag{7}$$

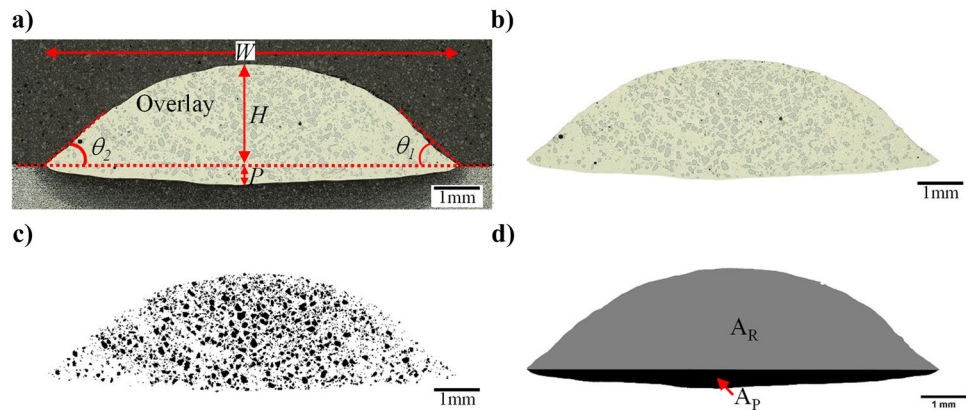
$$\eta (\%) = \frac{A_{\text{WC}} / A_R}{f_p} \tag{8}$$

ImageJ software was used to convert the optical images to binary images and to find the various areas of the carbide and the overlay (see Fig. 4c). As samples were lightly etched by 2% Nital, only retained and primary carbides can be easily identified by optical microscopy. They are not easily distinguishable, and both are captured during image processing. It should be

Table 5 Measured values of the tubular cored wire samples, used to calculate the f_p

Measured parameters	Sample 1	Sample 2	Sample 3	Sample 4	Sample 5	Average
Sample length [mm]	96.54	102.12	106.70	97.52	101.43	100.86
Electrode weight [g]	1.631	1.739	1.821	1.658	1.705	1.711
Powder weight [g]	0.892	0.958	0.995	0.904	0.921	0.934
l_m [g/mm]	0.0169	0.0170	0.0171	0.0170	0.0168	0.0170
$A_{\text{Ni-sheath}}$ [mm ²]	0.792	0.808	0.835	0.830	0.830	0.819
P_p [%]	54.68	55.08	54.63	54.52	54.01	54.58

Fig. 4 Typical overlay cross-section; **a** original image; **b** extracted overlay; **c** binary image of the carbides; **d** gray-scale dilution (A_R = reinforcement area; A_P = area of weld penetration; W = width; H = height; P = depth of penetration; θ_1 and θ_2 weld contact angle)



noted that the amount of primary carbides is small compared to that of retained carbides.

Dilution is due to a small portion of base material being mixed with the deposited material. Based on cross-section characterization as illustrated in Fig. 4d, DL is calculated using Eq. (9). For this purpose, Adobe Photoshop was used to separate reinforcement and penetration areas, followed by ImageJ software to calculate these areas of the overlay cross-section. It should be mentioned that, while calculating η using Eq. (8), the dilution effect is eliminated.

$$DL (\%) = A_P / (A_R + A_P) \quad (9)$$

2.4 Taguchi's signal-to-noise ratio

In Taguchi design, the signal-to-noise (S/N) ratio reflects how a response (i.e., a quality criterion) fluctuates with a process control parameter (signal) under varying noise conditions (other factors). The goal of quality criteria can be described as follows: larger the better, nominal the best, and smaller the better [43]. In this paper, the larger the better is selected as the goal of experiments for f_{WC} , η , DR , and W/H . For the DL and P , smaller the better is selected as the goal of the experiments. Accordingly, the S/N ratios for selected responses are calculated based on the formulas listed in Table 6. In general, higher S/N ratio

levels indicate that a control parameter has a larger influence on the outcome (response) and/or that it minimizes the influence of noise components. Minitab 20.3 software was utilized to obtain the means of mean plots and means of S/N ratio plots.

3 Results and discussion

3.1 Characterization of Ni-WC tubular cored feed wire

X-ray diffraction (XRD) patterns of the sheath of the feed wire and cored powder are presented in Fig. 5, and the corresponding SEM micrographs are shown in Fig. 6. The wire sheath consists of Ni alloy with Ni_3Si and Ni_2B precipitates. Boron and silicon elements are usually added to reduce the melting point and improve the self-fluxing ability of the matrix [44]. Table 7 lists EDS spot measurement results of the core particles at the locations indicated in Fig. 6. The results show the presence of angular shape tungsten carbide (points 3, 5, 11, 12, 14, 15, and 17), Ni-rich (points 1, 6, 8, 9, 10, 13, and 16), Si-rich (points 4, 7, 18, and 19), and Cr-rich (point 2) particles. Based on XRD analysis, these particles are identified to be mono-crystalline tungsten carbide (WC), NiB, Si, and Cr_3C_2 , respectively. In general, the particles/powders in the core of the feed wire consist of

Table 6 Summary of the selected goal for quality criteria of the overlay and corresponding S/N ratio formula

Quality criterion	Goal of experiments	S/N ratio* formula
f_{WC} η DR W/H	Larger-the-better (maximize the response)	$S/N = -10 \times \log(\Sigma(\frac{1}{Y_i^2})/n)$
DL P	Smaller-the-better (minimize the response)	$S/N = -10 \times \log(\Sigma(Y_i^2)/n)$

n = number of response's observations in each experiment

Y_i = observed measurement for each response

* The unit of the S/N ratio is decibels-isotropic (dBi)

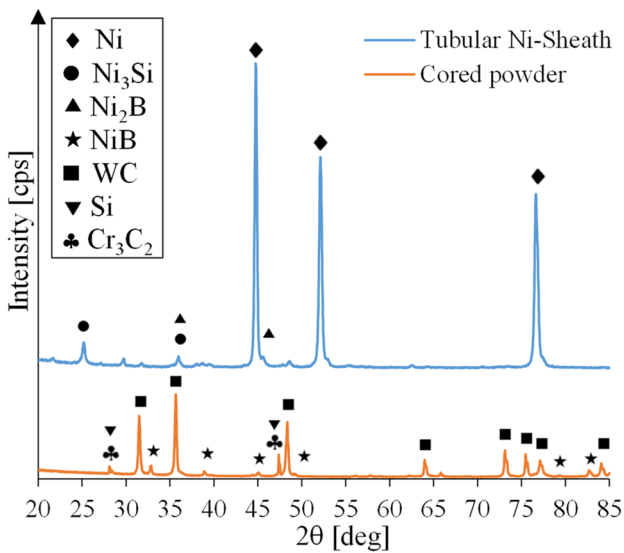


Fig. 5 XRD patterns of tubular wire sheath and cored powders

tungsten carbide particles and additional powders of alloying elements and/or fluxing agents. Mono-crystalline WC is normally fabricated by carburizing the conventional eutectoid W_2C/WC particle (~3.7 to 4.1 wt.% carbon) at elevated temperature to increase its carbon content to 6.1 wt.%. The mono-crystalline WC is more resistant to dissolution [10] and has better thermal stability [45] compared to eutectoid W_2C/WC . However, they have lower hardness (1200–2100 HV) [5].

3.2 Non-wetting behavior of powders during deposition

A considerable amount of black residue is observed across the whole weld region for all samples. Figure 7a shows the top view of one of the bead-on-plate samples, including the black residue. Figure 7b–d show some SEM micrographs, and Table 8 lists EDS spot measurement results of some particles/locations (as indicated in Fig. 7b–d) of the residue.

The black residue consists of Ni-rich sphere droplets due to spattering (point 6), irregular Ni-rich particles (points 3, 4, 5, 7, 11, and 16), mono-crystalline WC particles (points 1, 8, 9, 14, and 15), and oxidized W–Ni–C particles (points 2, 10, 12, and 13). The existence of WC in the black residue is direct evidence of WC losses during the weld cladding process, resulting in lowered f_{WC} in the resultant overlay as compared to f_p , as also observed by other studies of weld cladding of related overlays [23]. WC particles with no signs of melting and retaining their original shape show a very low concentration of Ni, indicating poor wettability of these particles with the molten droplet/pool. During deposition, some loose particles from the powder can fall and hit the weld pool. Depending on the impingement velocity of these particles, they might be unable to overcome the surface tension of the molten pool and therefore bounce off or sit on top of the molten pool surface and are further ejected by arc re-ignition [22]. It should be mentioned that all EDS measurements indicate high concentrations of oxygen, which is due to the oxidation of particles during the deposition process.

Fig. 6 a SEM image of the cross-section of the tubular Ni-WC cored wire; b selected area in a at higher magnification; c powders taken out of the core of the feed wire; d selected area in c at higher magnification (with the numbers indicating the locations of EDS spot measurements)

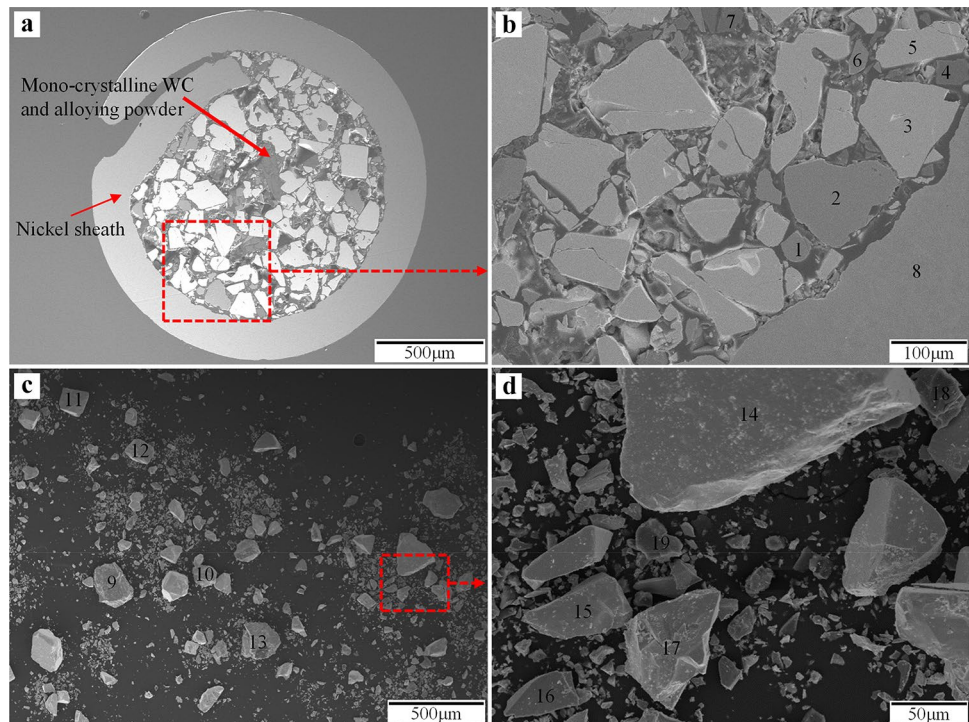


Table 7 EDS spot measurement results of marked locations in Fig. 6

Elements (wt.%)	Point																		
	1	2	3	4	5	6	7	8	9	10	11	12	13	14	15	16	17	18	19
C	6.16	3.68	9.11	8.98	9.55	5.87	10.56	5.57	9.44	11.23	12.91	11.49	7.84	9.05	9.22	5.41	11.39	11.84	14.5
O	0.12	2.34	0.55	0.39	0.76	0.05	0.77	0.71	0.00	1.41	1.02	1.49	2.04	1.09	0.88	0.31	1.82	1.33	0.95
Si	0.04	0.18	0.00	90.11	0.00	0.16	88.37	0.08	0.06	0.39	0.00	0.00	0.33	1.36	0.00	0.39	3.72	85.21	84.29
Cr	0.24	93.61	0.09	0.00	0.00	0.00	0.03	0.00	0.01	0.03	0.06	0.01	0.07	0.09	0.04	0.00	0.00	0.05	0.00
Fe	0.14	0.06	0.21	0.00	0.03	0.13	0.00	0.06	0.05	0.21	0.14	0.24	0.24	0.02	0.52	0.13	4.54	0.00	0.00
Ni	93.3	0.13	0.09	0.51	0.02	93.79	0.28	93.59	90.31	83.56	0.17	0.15	86.82	0.88	0.26	89.96	1.06	0.25	0.25
W	0.00	0.00	89.95	0.00	89.63	0.00	0.00	0.00	0.14	3.16	85.71	86.61	2.66	87.52	89.09	3.8	77.47	1.31	0.00

Guest [20, 22] illustrated the non-wetting behavior of WC by high-speed camera images during a standard GMAW process. They observed the non-wetting behavior of WC in all metal transfer modes and reported a minimum of 20% loss of WC because of this loss mechanism. In this work, the EDS results on the black residues indicate the existence of this loss mechanism in the CMT process as well. However, it should be pointed out that material transfer mode in CMT process is controlled by the mechanical detachment of droplets, which is fundamentally different from the standard GMAW process. The related behavior during CMT process will be investigated further in future studies using high-speed camera.

3.3 Effect of processing parameters on the quality of Ni-WC MMC overlays

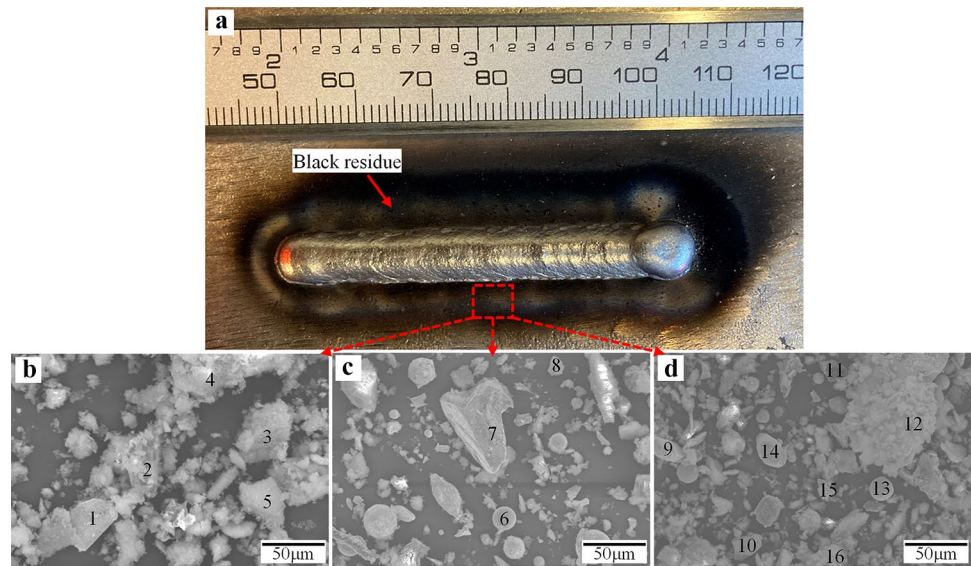
Figure 8 presents the top views and images of cross-sections of all single weld bead tracks. As can be seen, the bead profiles are continuous and uniform with low spatter. The cross-sections exhibit excellent metallurgical bonding to the substrates without crack, low porosity level, and relatively uniform distribution of the retained WC. These cross-sectional images provide the required information to determine f_{WC} , η , and weld bead characteristics (DL , P , H , W , W/H , and θ), which are summarized in Table 9. The average porosity of all samples is 1.42%, while only four samples have the porosity greater than 2% (samples 1, 3, 4, and 8). The HI for these four samples is low (between 0.09 and 0.19 kJ/mm); sample 2 is also related to low HI (0.15 kJ/mm), but has low porosity level of 1%.

3.3.1 Effect of processing parameters on material transfers and weld bead characteristics

Figure 9a and b show the mean influence of processing parameters on f_{WC} and η , respectively. It can be seen that increasing the WFS and TS leads to a reduction of f_{WC} and η . Higher WFS involves higher current as indicated in Table 3, which increases AIP and thus arc energy, facilitating WC dissolution. The observation that increased TS leads to a reduction of f_{WC} and η is not in line with previous studies by other authors using standard GMAW processes, where higher TS was linked to lower HI and thus lower dissolution of WC [20, 46]; as discussed below, the effect of TS may be more complicated in the present study.

It should be noted that η is generally undervalued, depending on the level of WC dissolution. The concept for f_{WC} and η calculation is based on the assumption that all the retained WC in a weld bead track could be accounted for in the calculation. In reality, WC is inevitably partially dissolved. The image processing is arranged so that only retained WC and primary WC (formed during solidification)

Fig. 7 **a** Black residues around weld bead after deposition; **b–d** SEM images of black residues



can be captured for f_{WC} and η evaluations. The capture of primary WC for η evaluations will compensate for the effect of dilution to a certain degree. However, all the secondary carbides are not accounted for by proper image processing, as they are mostly W-rich carbides containing Fe or Ni.

The level of CO_2 in the SG mixture does not seem to have a significant effect on f_{WC} and η . However, f_{WC} and η are observed to increase with an increasing level of O_2 in the SG. Improvements in η by O_2 addition to the SG have previously been documented [22]. The addition of a controlled amount of oxidizing gas, such as CO_2 or O_2 , to an Ar-rich SG mixture, can modify the thermophysical characteristics of plasma arc, improving welding arc stability, heat transfer, surface tension, and weldability [47–49]. Nevertheless, CO_2 addition to the SG seems to be much less effective in achieving arc stabilization as compared to O_2 addition for depositing the Ni-WC material system. Molten nickel resists oxidation, leading to fewer electron emissions and reducing stability at the cathodic locations. O_2 addition in SG effectively promotes the oxidation of the nickel weld pool, improving arc stability during the droplet formation period

[20]. Improved arc stability leads to increased η and, thus, increased f_{WC} .

It can be observed in Fig. 9c–f that WFS is the main controlling factor for weld bead characteristics and DR . WFS determine DR , as it directly dictates the feeding rate of cored feed wire. Higher WFS also leads to higher arc energy, resulting in an increase in substrate melting (directly increasing P , DL , and WH) and, thus, having a significant effect on weld bead characteristics. Higher TS also increases DL , P , and WH , but its effect on DR is only marginal.

The effect of TS on P and DL can be understood by considering the combined effect of HI and arc impingement. According to Silva [50], P and DL are positively correlated with HI , but inversely correlated to impingement effect. At sufficient low TS , the impingement effect dominates, where the arc impinges on the weld pool rather than the substrate and the metal deposited acts as a barrier preventing direct arc impingement on the base metal; as such, lower P and DL are achieved at lower TS for the resultant overlay [30]. P and DL increase with increased TS until it reaches a critical point, after which the effect of HI dominates, and P and DL

Table 8 EDS spot measurement results of marked locations in Fig. 7

Elements (wt.%)	Point															
	1	2	3	4	5	6	7	8	9	10	11	12	13	14	15	16
C	7.58	15.88	7.34	8.52	10.38	6.07	9.97	12.37	16.23	16.28	2.33	9.51	18.1	5.87	7.63	7.7
O	7.40	18.93	6.50	10.7	13.73	3.21	6.38	1.74	5.9	13.02	10.86	16.07	14.2	11.83	9.76	8.3
Si	0.50	1.62	1.24	4.19	1.30	1.14	1.39	0.00	0.35	5.19	2.75	2.19	2.8	0.25	0.74	1.76
Cr	0.10	0.29	0.57	0.77	0.56	0.25	0.27	0.00	0.11	0.17	0.5	0.32	0.45	0.06	0.08	0.85
Fe	0.54	39.16	2.18	1.86	1.56	0.67	0.60	0.35	0.35	0.75	1.48	0.83	1.3	0.18	0.43	2.07
Ni	6.06	21.37	79.18	60.54	69.87	77.05	78.89	3.75	7.55	20.44	65.04	21.34	36.08	3.04	5.96	69.86
W	77.81	2.77	2.98	13.4	2.59	11.61	2.51	81.79	69.51	44.16	17.06	49.74	27.07	78.76	75.4	9.47



Fig. 8 Top and cross-sectional views of the specimens

decrease with increased TS . As indicated in Fig. 9c and d, the critical TS could be around 0.5 m/min.

As shown in Fig. 9c and f, DL and WH remain almost unchanged when using SG mixture with CO_2 addition;

however, O_2 addition in the SG results in relatively lower DL and WH . This is due to the change of thermophysical characteristics of the plasma arc, resulting in reduced surface tension of the weld pool, enhancing the wettability of the weld pool

Table 9 Experimental results summarizing processing, carbide, and weld bead characteristics of all specimens

ID	WFS [m/min]	TS [m/min]	SG [%]	I_{avg} [A]	V_{avg} [V]	HI [kJ/mm]	AIP [kW]	f_{WC} [%]	η [%]	DL [%]	P [mm]	DR [kg/h]	W [mm]	H [mm]	W/H	θ [°]
1	2.1	0.3	25% CO ₂	62.89	10.53	0.19	0.93	25.2	67.1	0.92	0.04	1.20	3.84	2.17	1.77	80
2	2.1	0.4	15% CO ₂	64.38	10.46	0.15	0.98	26.8	71.4	1.05	0.07	1.30	3.37	2.02	1.67	85
3	2.1	0.5	2% O ₂	64.37	8.97	0.10	0.85	20.7	55.5	1.65	0.09	1.28	1.92	2.06	0.93	122
4	2.1	0.6	5% O ₂	63.45	9.33	0.09	0.87	24.5	65.4	0.88	0.06	1.28	3.35	1.46	2.30	71
5	3.9	0.3	15% CO ₂	94.78	10.90	0.29	1.46	25.7	74.2	8.52	0.27	1.87	7.10	2.05	3.47	49
6	3.9	0.4	25% CO ₂	93.09	12.03	0.25	1.66	20.7	64.2	14.83	0.25	1.89	6.82	1.68	4.05	41
7	3.9	0.5	5% O ₂	91.24	9.82	0.16	1.36	23.0	65.2	6.77	0.15	2.01	6.00	1.67	3.60	50
8	3.9	0.6	2% O ₂	92.39	9.33	0.13	1.32	18.6	52.4	6.57	0.18	1.95	5.35	1.60	3.34	49
9	5.7	0.3	2% O ₂	127.78	9.46	0.35	1.75	27.5	78.0	6.93	0.19	2.40	7.70	2.28	3.37	49
10	5.7	0.4	5% O ₂	129.84	10.12	0.28	1.89	22.4	68.3	13.64	0.35	2.50	7.93	1.83	4.34	36
11	5.7	0.5	25% CO ₂	140.47	12.68	0.30	2.54	18.9	62.8	20.72	0.29	2.55	6.92	1.56	4.43	34
12	5.7	0.6	15% CO ₂	139.90	11.75	0.24	2.36	12.0	38.1	16.99	0.37	2.79	7.66	1.57	4.88	32
13	7.5	0.3	5% O ₂	166.34	10.30	0.47	2.34	26.3	77.4	10.08	0.42	3.03	9.86	2.40	4.11	43
14	7.5	0.4	2% O ₂	165.06	9.39	0.32	2.14	26.2	78.1	11.67	0.32	3.04	7.99	2.18	3.67	49
15	7.5	0.5	15% CO ₂	177.05	11.77	0.34	2.86	18.2	60.7	20.83	0.55	3.40	9.83	1.78	5.52	30
16	7.5	0.6	25% CO ₂	173.29	12.27	0.29	2.95	10.3	34.1	20.26	0.44	3.15	8.64	1.58	5.46	27

and heat transfer, leading to shallower P (i.e., lower DL), and altering the weld bead geometry [47–49]. SG compositions do not show any significant effect on the DR , as seen in Fig. 9e.

Figures 10 and 11 illustrate the effect of HI and AIP on f_{WC} , η , DR , and weld bead characteristics, respectively. The data in these graphs are fitted by a linear function; R^2 (shown in each plot) is a measure of overall closeness of the data to the fitted regression line; the larger the R^2 value (between 0 and 1), the better the linear regression fitting. No meaningful correlation can be identified between f_{WC}/η and HI/AIP , which is in contrast to the observation for standard GMAW processes where f_{WC} is negatively correlated with HI [11, 51]. It seems that the most important factor for determining f_{WC} or η in the current study is the TS , with WFS being the second most important factor, as indicated in Fig. 9. Although HI or AIP varies with changing WFS for a CMT synergic mode, their effects on f_{WC} or η may not be fully interconnected, as other factors (such as TS) also play a role here. It is interesting to notice that high level of f_{WC} or η can be accomplished even at high HI , where high DR and good weld bead appearance are also achieved. Vespa et al. [18] indicated a similar trend using controlled short-circuit GMAW process, which is comparable to the CMT process but with less complex waveform control.

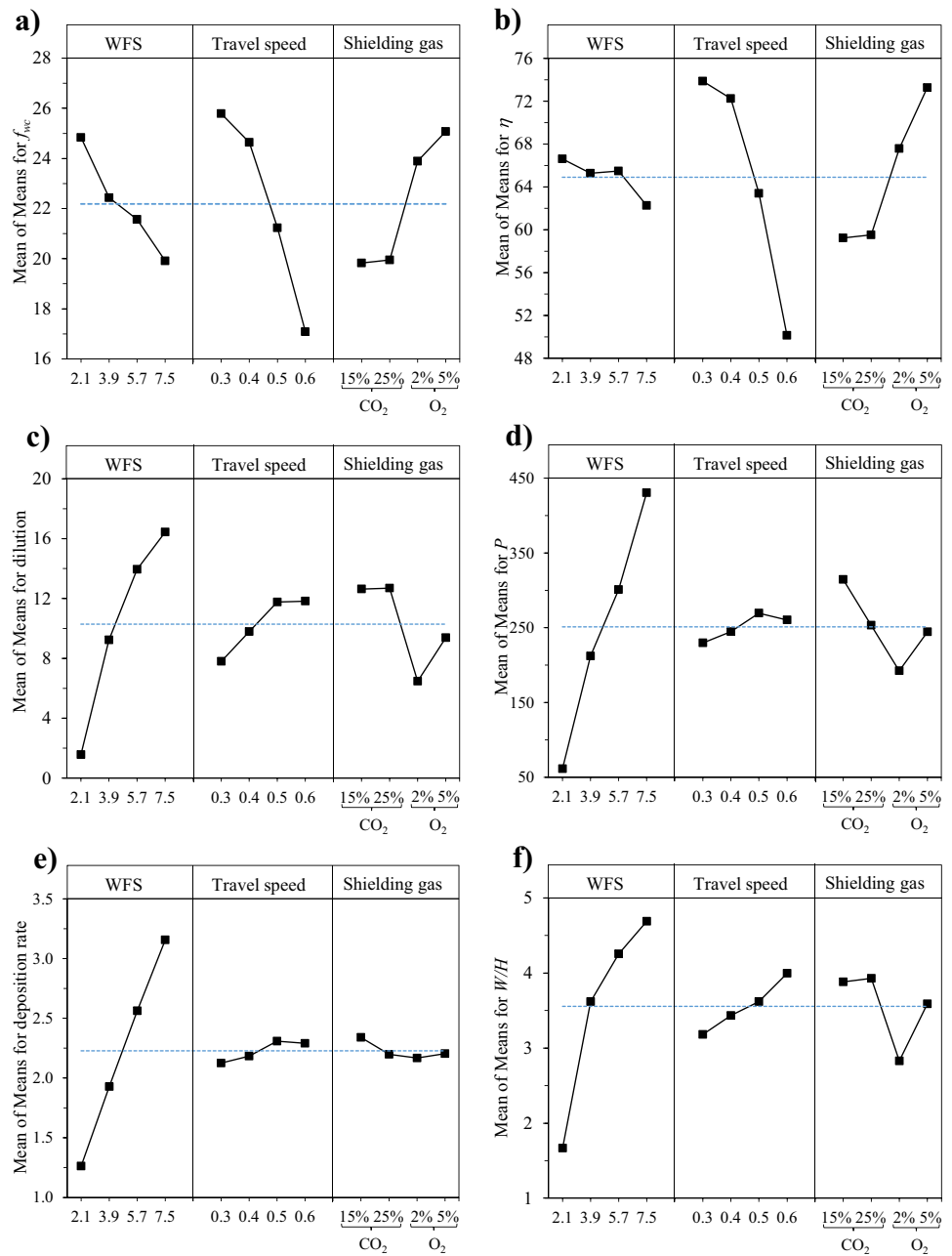
As shown in Figs. 10c–f and 11c–f, DR , DL , P , and W/H exhibit, in general, a positive correlation with HI or AIP , respectively. This correlation seems to be more pronounced for AIP as compared to HI , which was observed by other researchers as well [30, 52]. Moreover, the results also support the assumption that AIP can be a better governing factor to control weld bead characteristics and DR than HI , as suggested by other authors [19, 52].

As indicated in Fig. 12, a generally negative correlation can be identified between DL and f_{WC} . The results suggest that f_{WC} of above 20% are achieved at DL below 5%. However, in cases of higher DL (> 15%) related to high WFS (5.7–7.5 m/min) and high TS (0.6 m/min), the amount of f_{WC} is drastically reduced. The same behavior was reported by Günther and Bergmann [46], who showed that high DL is directly related to the higher concentration of Fe migrated into the overlay from the substrate, leading to the excessive dissolution of WC.

3.3.2 Effect of processing parameters on microstructures

Samples 3, 7, 10, and 16 were analyzed to evaluate the effect of processing parameters on the microstructure; the related AIP for deposition of these specimens is 0.85, 1.36, 1.89, and 2.95 kW, respectively. Figures 13, 14, 15, 16, 17, 18, and 19 show the micrographs of these samples taken from the whole overlay area. EDS spot measurement results of the selected areas are presented in Tables 10, 11, 12, and 13.

Fig. 9 Main effect plots for **a** f_{WC} ; **b** η ; **c** DL ; **d** P ; **e** DR ; **f** W/H (with dash lines indicating means)

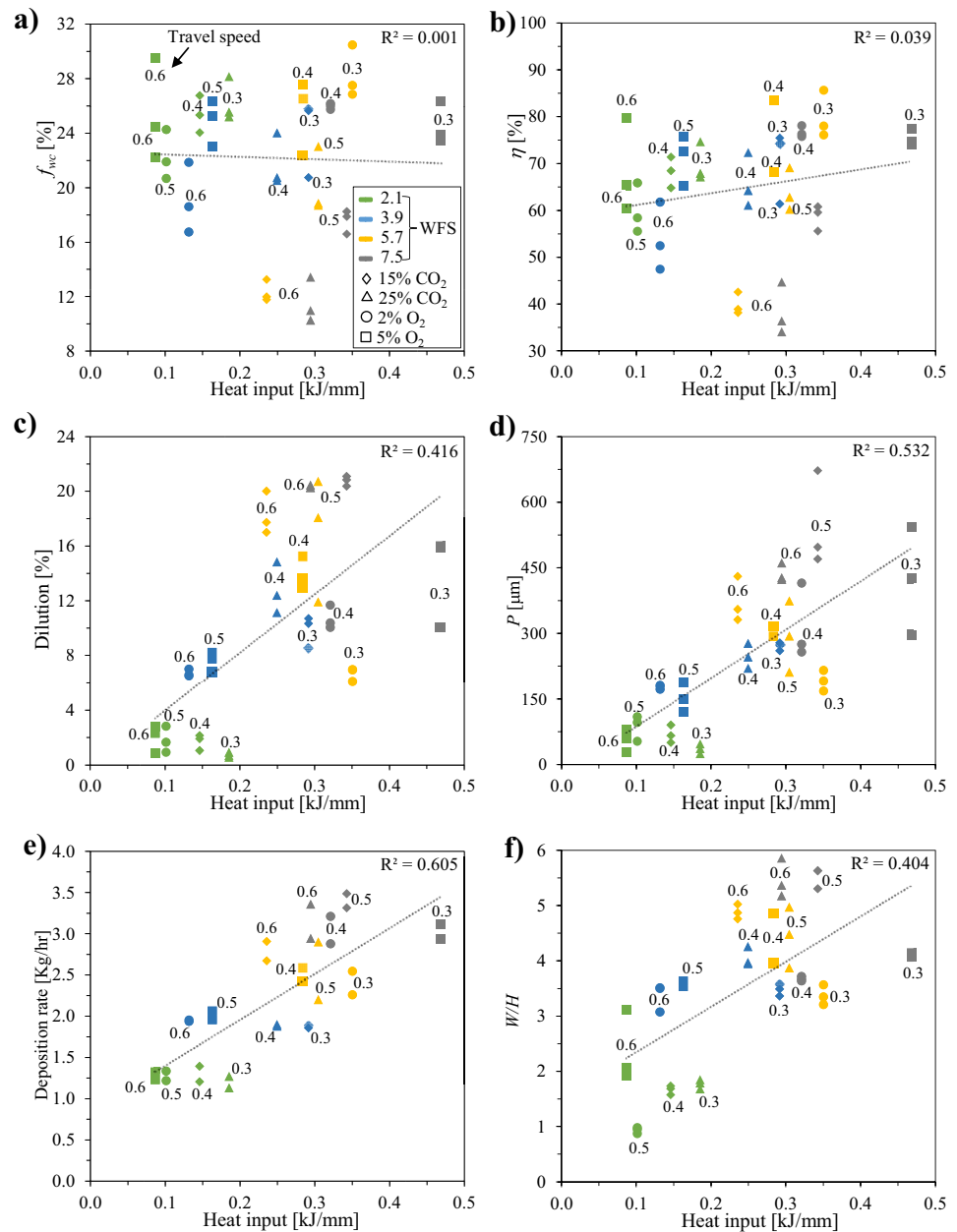


Microstructure characterization of sample 3 (AIP: 0.85 kW) The matrix is composed of a light gray phase (e.g., points 1 and 13 in Fig. 13) and a dark gray phase (e.g., points 2 and 14). EDS results show a high concentration of Ni, varying from 73.94 to 77.49 wt.%, see Table 10. The matrix microstructure is similar to a conventional Ni-based matrix microstructure, as also indicated by Liyanage et al. [9]; hence, the light and dark gray phases are characterized as γ -Ni dendrites and γ -Ni + Ni_3B interdendritic eutectic region, respectively. Because of the higher temperature gradient near the interface between the substrate and overlay [53, 54], the planar crystal layer is formed first near the interface, followed by columnar γ -Ni dendrites along the solidification path,

as illustrated in Fig. 13a and b. The EDS maps of the substrate/overlay interface show a visible diffusion zone of migrated Fe from the substrate into the overlay, indicating a good metallurgical bond (see Fig. 14). By moving towards the top of the overlay, the concentration of Fe gradually decreases, as confirmed by EDS results (see Table 10) with Fe concentration of 4.92–5.31 wt.% at the interface (points 1 and 2) and 1.3–1.39 wt.% (points 13 and 14) at the top of the overlay.

A degradation seam is not observed around the retained WC particles. They show an excellent metallurgical bond to the adjacent matrix, in contrast to the cases with retained WC/ W_2C eutectic particles around which a degradation

Fig. 10 Effect of *HI* on quality criteria: **a** f_{WC} ; **b** η ; **c** *DL*; **d** *P*; **e** *DR*; **f** *W/H*

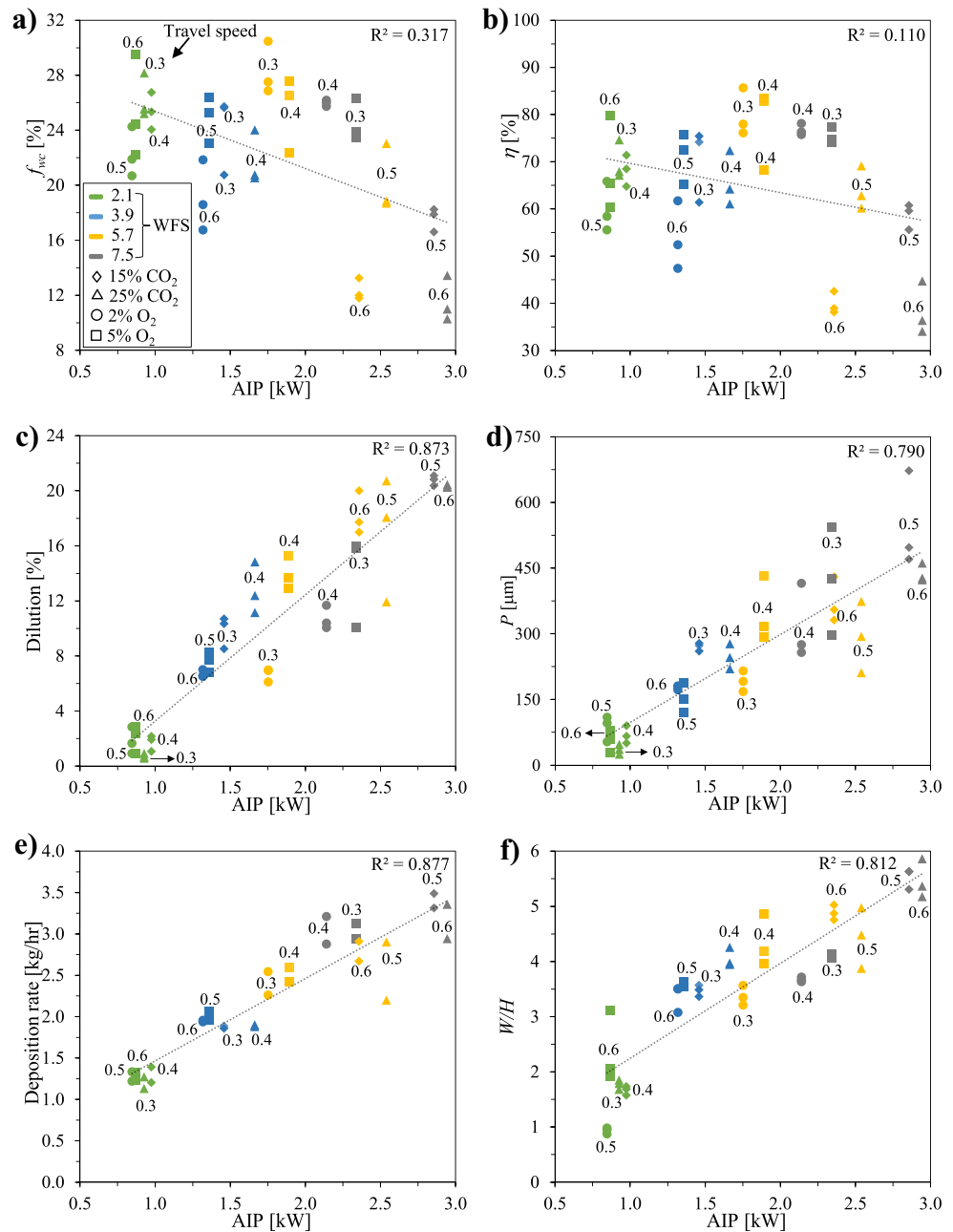


seam usually forms due to preferential dissolution of W_2C (as W_2C is less stable than WC) [19, 55]. Nevertheless, the mono-crystalline WC particles can inevitably partially dissolve in the molten pool during deposition, increasing the concentration of W in the Ni -based matrix (see Table 10, points 1, 2, 13, and 14).

Small precipitates are found within the γ - Ni dendrites (see Fig. 13b and c). These homogeneously formed precipitates ($< 15 \mu m$) have triangle and rectangle morphologies presence throughout the whole thickness of the overlay, as also observed by Zhao et al. [55]. EDS analysis results on these precipitates (see Table 10, points 3–6) indicate high W and C concentrations ranging from 69 to 72 wt.% and 18

to 21 wt.%, respectively; therefore, these tiny particles can be identified as primary WC precipitates formed from free W and C (due to dissolution of WC particles) in the molten pool during the solidification process, as also reported in previous literature [16, 18, 42, 55]. The formation of primary WC can be realized by considering the C -rich side of the Ni - W - C ternary phase diagram [56], where WC grains develop into a three-dimensional triangular prism via a layer-by-layer growth mechanism. Random cross-sectioning of primary WC triangular prism [57] is responsible for the different morphology observed, varying from equilateral triangles, isosceles triangles, and irregular triangles to quadrilaterals [42].

Fig. 11 Effect of AIP on quality criteria: **a** f_{WC} ; **b** η ; **c** DL ; **d** P ; **e** DR ; **f** W/H



Black semi-spherical precipitates are observed in Fig. 13c and f. EDS result at point 7 reveals that this precipitate is rich in carbon. The same black semi-spherical precipitates were reported in laser cladding deposition of Ni-WC MMCs on carbon steel [16] or cast iron substrate [58]. Using bright field transmission electron microscopy, Zhao et al. [16] characterized these precipitates as incompletely graphitized residual carbon formed due to the rapid solidification process. According to the Ni–C binary phase diagram [59], there is only a limited solubility of carbon into nickel, and γ -Ni + graphite + WC three-phase can be thermodynamically stable at certain elevated temperatures [18, 56]. Therefore,

under high cooling rates, graphite precipitates could be retained in the overlay at room temperature [16, 18, 58].

As shown in Fig. 13d–i, moving from the lower to the upper region of the overlay, the microstructure remains relatively unchanged; this may be due to lower HI (resulting in higher thermal gradient and faster solidification rate), which suppresses overall phase transformation at low temperatures, enabling metastable phases retained at the room temperature. EDS results indicate that points 8–12 are WC. The microstructure consists of the retained WC, γ -Ni dendrites, γ -Ni + Ni₃B lamellar eutectic in the interdendritic region, primary WC, and graphite precipitates.

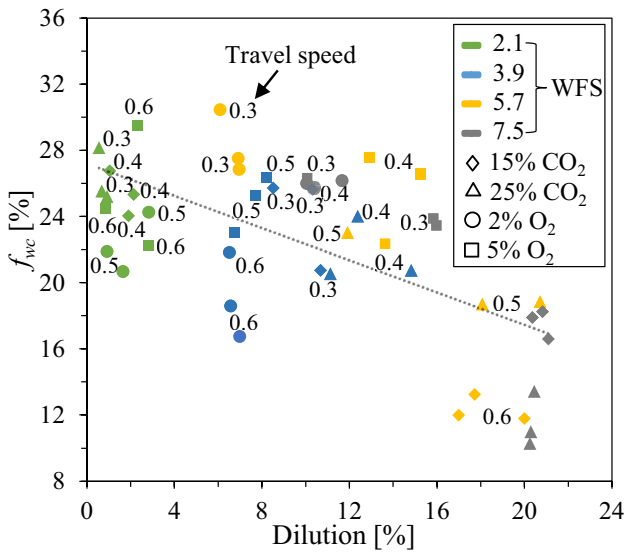


Fig. 12 Effect of DL on f_{WC}

Microstructure characterization of sample 7 (AIP: 1.36 kW) For sample 7, the matrix is also composed of γ -Ni dendrites (points 1 and 10 in Fig. 15) and γ -Ni + Ni_3B lamellar eutectic in the interdendritic region (points 2 and 11). Similar to sample 3, the substrate/overlay interface is identified by the planar crystal layer followed by columnar γ -Ni dendrites formed along the solidification path (see Fig. 15b and c). The EDS maps of the substrate/overlay interface show a visible diffusion zone of migrated Fe from the substrate into the overlay, indicating a good metallurgical bond (see Fig. 16a). According to Table 11 (EDS point results of marked locations in Fig. 15), the amount of dissolved Fe is 11.57–13.6 wt.% at the interface (points 1 and 2) and 7.92–9 wt.% (points 11 and 12) at the top of the overlay. Because of the increased DL , there is more dissolved Fe in sample 7 than in the matching regions of sample 3. The black precipitates are graphite uniformly distributed throughout the overlay.

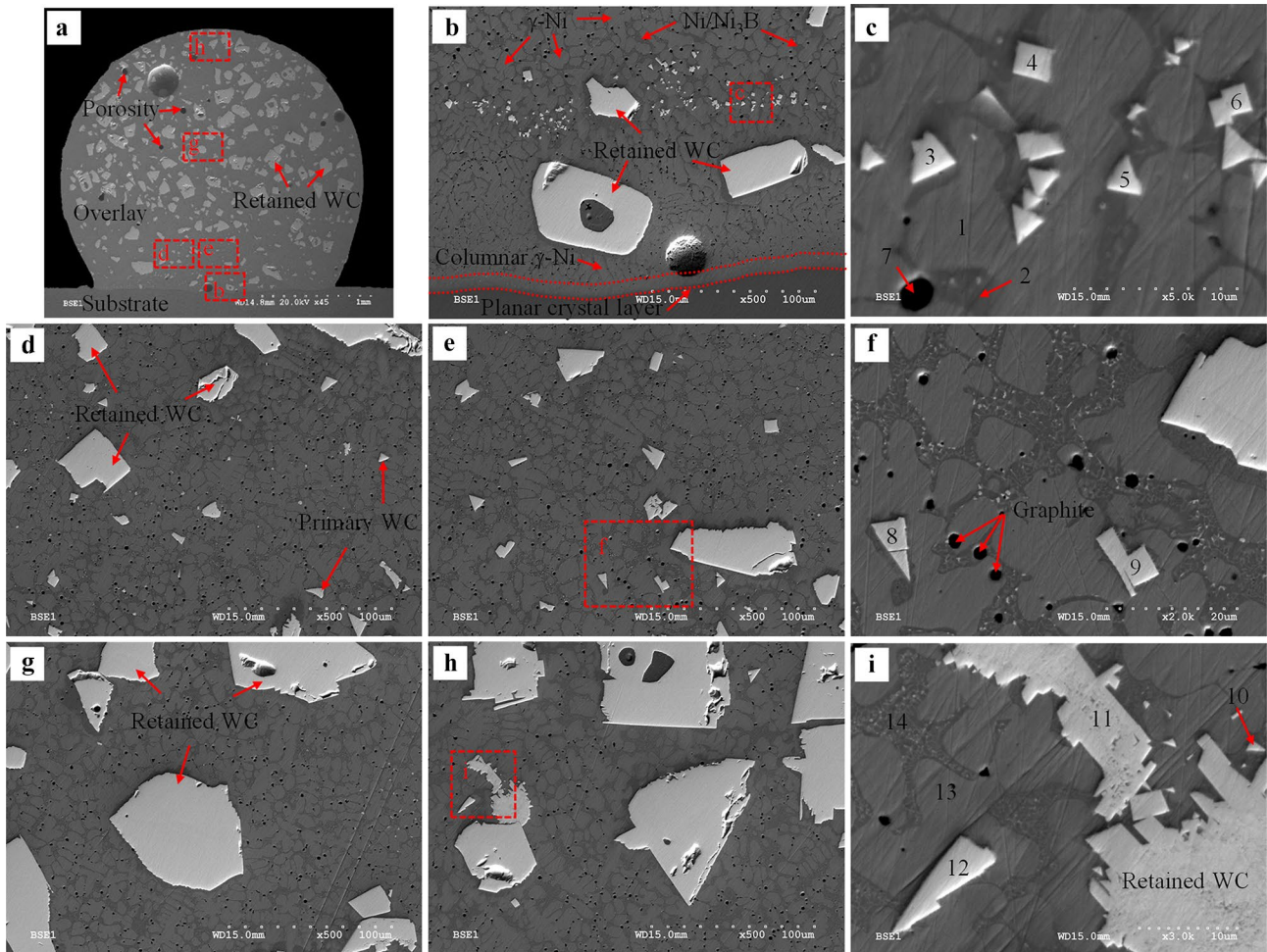


Fig. 13 BSE images of sample 3 (AIP: 0.85 kW): **a** overlay cross-section; **b** interface of the substrate/overlay; **c** higher magnification of the selected area in **b**; **d** and **e** lower region; **f** higher magnification of

the selected area in **e**; **g** middle region; **h** upper region; **i** higher magnification of the selected area in **h**

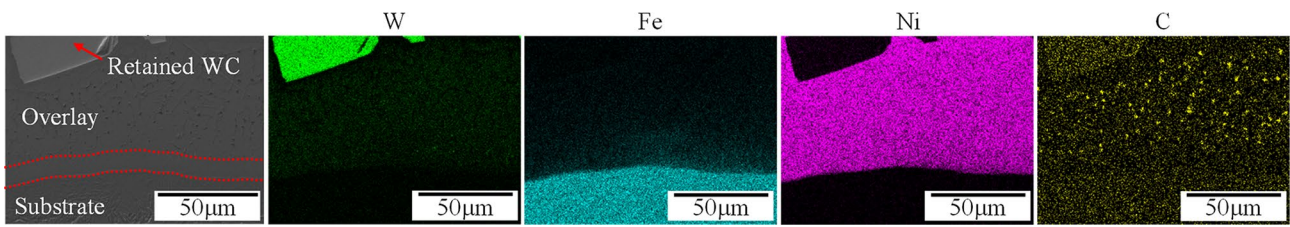


Fig. 14 EDS map of the interface of substrate/overlay of sample 3 (AIP: 0.85 kW)

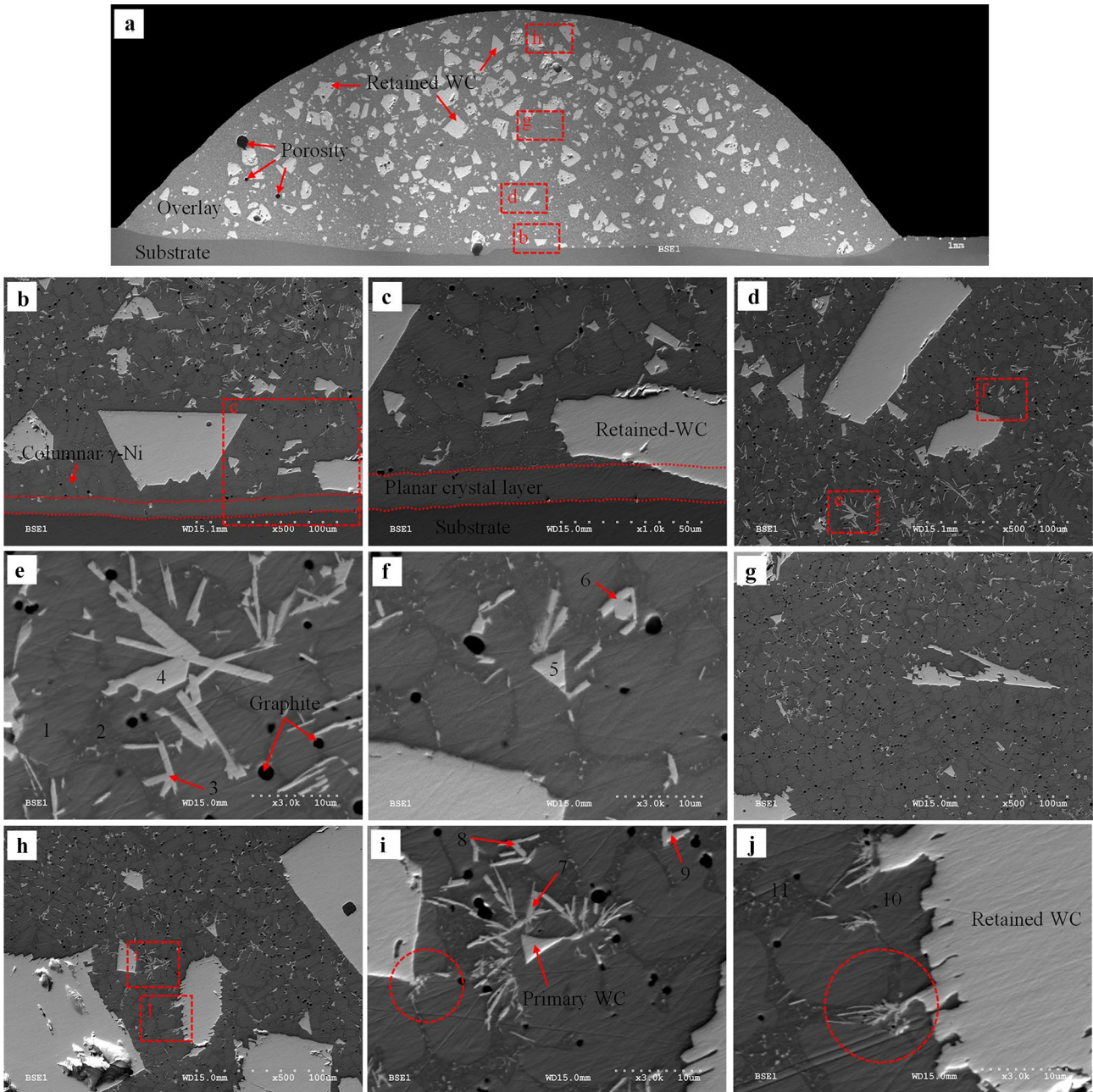


Fig. 15 BSE images of sample 7 (AIP: 1.36 kW): **a** whole overlay cross-section; **b** interface of the substrate/overlay; **c** higher magnification of the selected area in **b**; **d** lower region; **e** and **f** higher magnification of the selected area in **d**; **g** middle region; **h** upper region; **i** and **j** higher magnification of the selected area in **h**

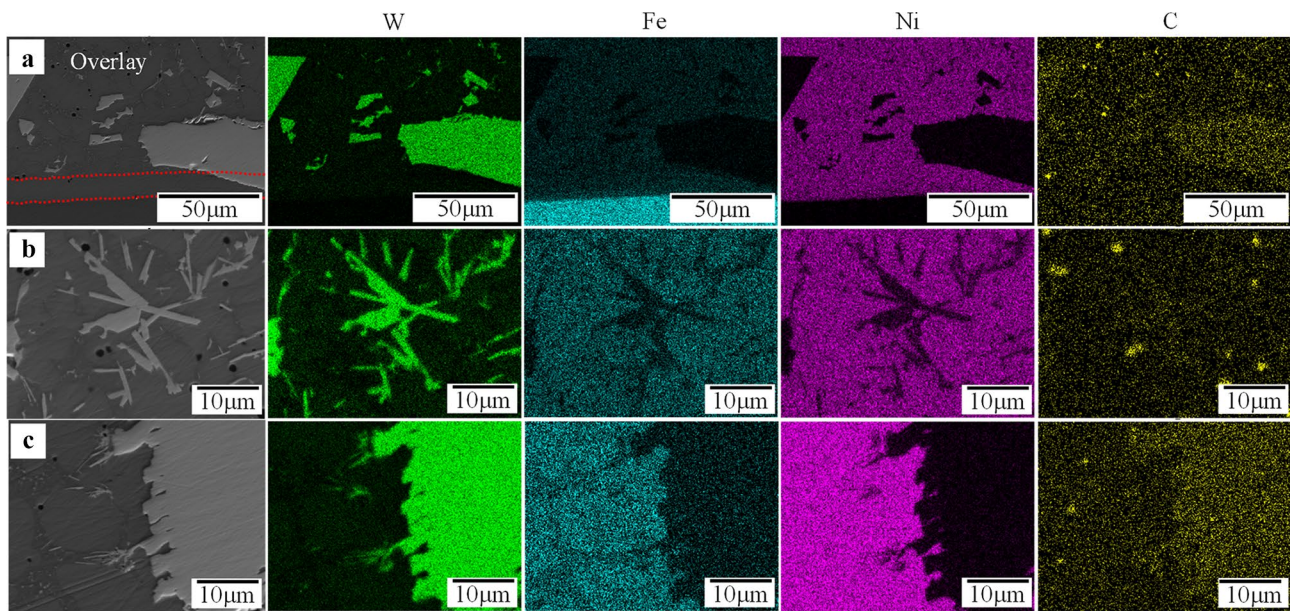


Fig. 16 EDS map of the cross-section of sample 7 (*AIP*: 1.36 kW): **a** interface of substrate/overlay; **b** secondary carbide at lower region; **c** selected area at upper region

Homogeneously formed precipitates of primary WC (i.e., point 5 in Fig. 15f) are detected. Moving from the lower to the upper region of the overlay, the formation of secondary W-rich carbides with the rod/grass-like (points 3, 6, and 7–9) and blocky (point 4) shapes are also detected, as shown in Fig. 15d–j. In reference to Zhao et al. [16], considering EDS analyses and the morphology of these carbides, the rod/grass-like ones may be identified as WC while the blocky ones as W_2C . The retained WC can provide heterogeneous nucleation sites for the secondary carbides, which may be promoted by the locally excessive W and C owing to partial WC dissolution; the secondary carbides can preferentially grow along the edges of the retained WC particles (see the marked area in Figs. 15i and j and 16c). Formation of these new phases and morphologies can also be realized due to higher *HI* and lower cooling rate [54].

Microstructure characterization of sample 10 (*AIP*: 1.89 kW) Sample 10 has a different microstructure than samples 3 and 7 due to higher *HI*, *AIP*, and *DL*, leading to a lower cooling rate which facilitates the formation of secondary W-rich carbides, as shown in Fig. 17. The main difference may be the formation of herringbone M_6C carbide at the interface, lower and middle region of the overlay. According to the EDS results (Fig. 18 and Table 12) and studies by other researchers [16, 42], points 1 and 2 can be characterized as Fe_3W_3C and points 6–8 as Ni_2W_4C . Furthermore, the diffusion zone at the substrate/overlay interface is wider than samples 3 and 7. EDS result of point 3

shows a higher concentration of dissolved Fe at a level of 24.6 wt.% (see Table 12), consistent with its higher *DL*. The microstructure at the middle to the upper region of the overlay matrix mainly consists of γ -Ni dendrites, γ -Ni + Ni_3B lamellar eutectic, newly formed WC with triangles/quadrilaterals or rod/grass-like morphology (points 9, 10, 13, and 14).

Microstructure characterization of sample 16 (*AIP*: 2.95 kW) Sample 16 shows a notable microstructural difference from other characterized samples due to its highest *DL* and *AIP* (resulting in the lowest thermal gradient and cooling rate), which facilitates the dissolution of WC in the molten pool and solid phase transformation during the cooling process. Apart from the detected microstructure discussed in previous samples, secondary carbides are observed with various additional morphologies, including herringbone, flower-like, and petal-like ones, as shown in Fig. 19. Herringbone precipitates formed throughout the whole overlay, which is attributed to the higher dwell time of the molten pool. According to the EDS results (Fig. 20 and Table 13), point 4 may be identified as Fe_3W_3C and points 9–11 likely as Ni_2W_4C . Furthermore, flower and petal-like carbides (points 1–3) are rich in W and are likely W_2C [60]. Primary WC is observed as rod-like precipitates (points 5 and 6) or triangles/quadrilaterals (points 7 and 8). The formation of Fe_3W_3C is plausible even in the upper region of the overlay due to available Fe at a level of 22.31 to 22.51 wt.% in the matrix (see points 12 and 13 in Table 13).

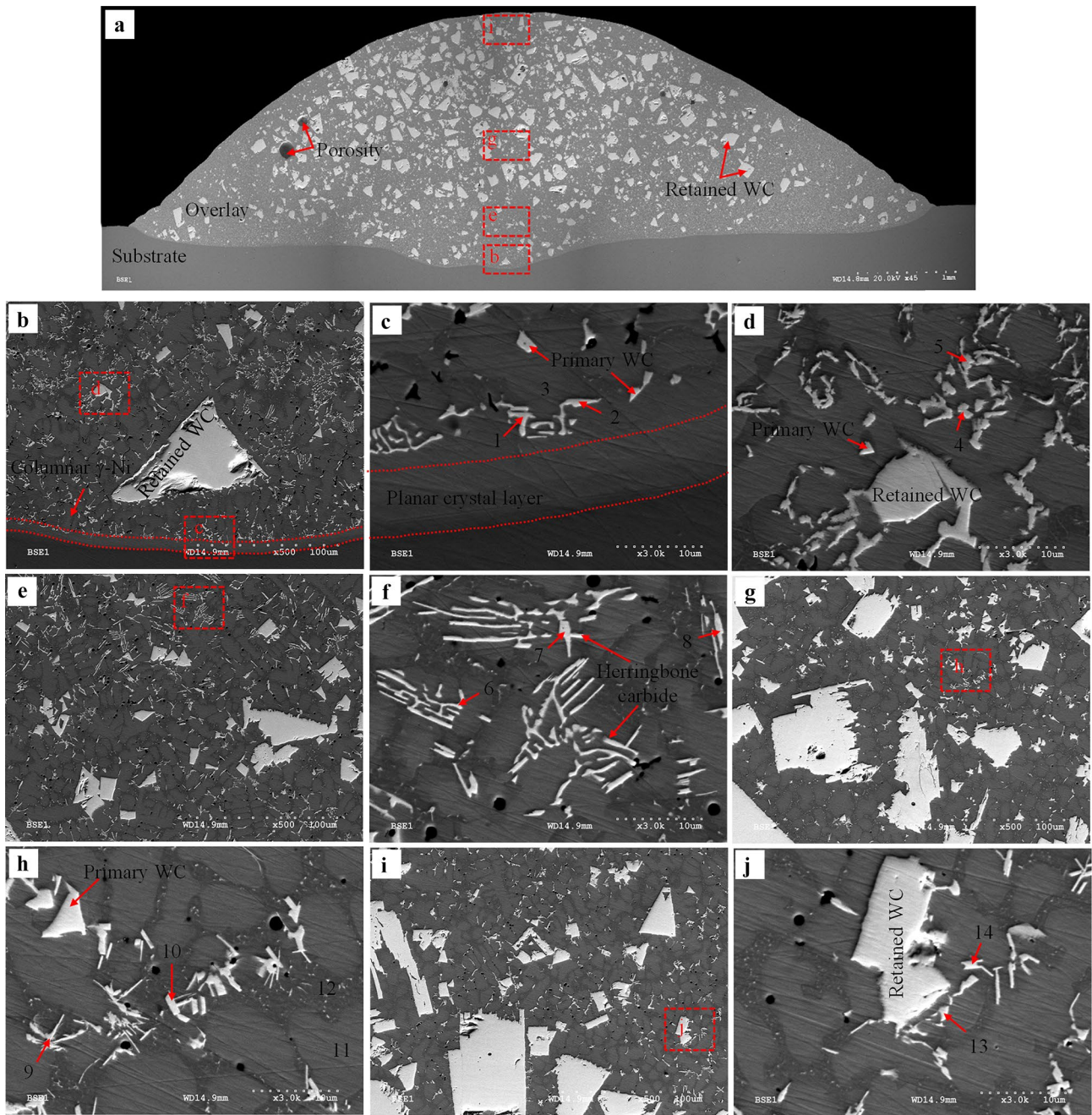


Fig. 17 BSE images of sample 10 (*AIP*: 1.89 kW): **a** overlay cross-section; **b** interface of the substrate/overlay; **c** and **d** higher magnification of the selected area in **b**; **e** lower region; **f** higher magnification

of the selected area in **e**; **g** middle region; **h** higher magnification of the selected area in **g**; **i** upper region; **j** higher magnification of the selected area in **i**

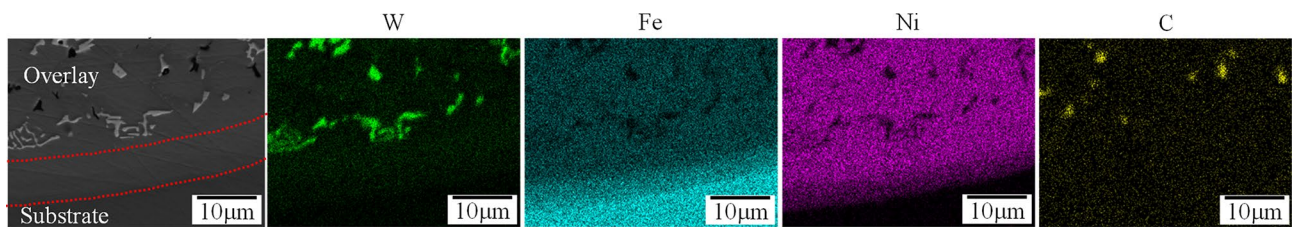


Fig. 18 EDS map of the interface of substrate/overlay of sample 10 (*AIP*: 1.89 kW)

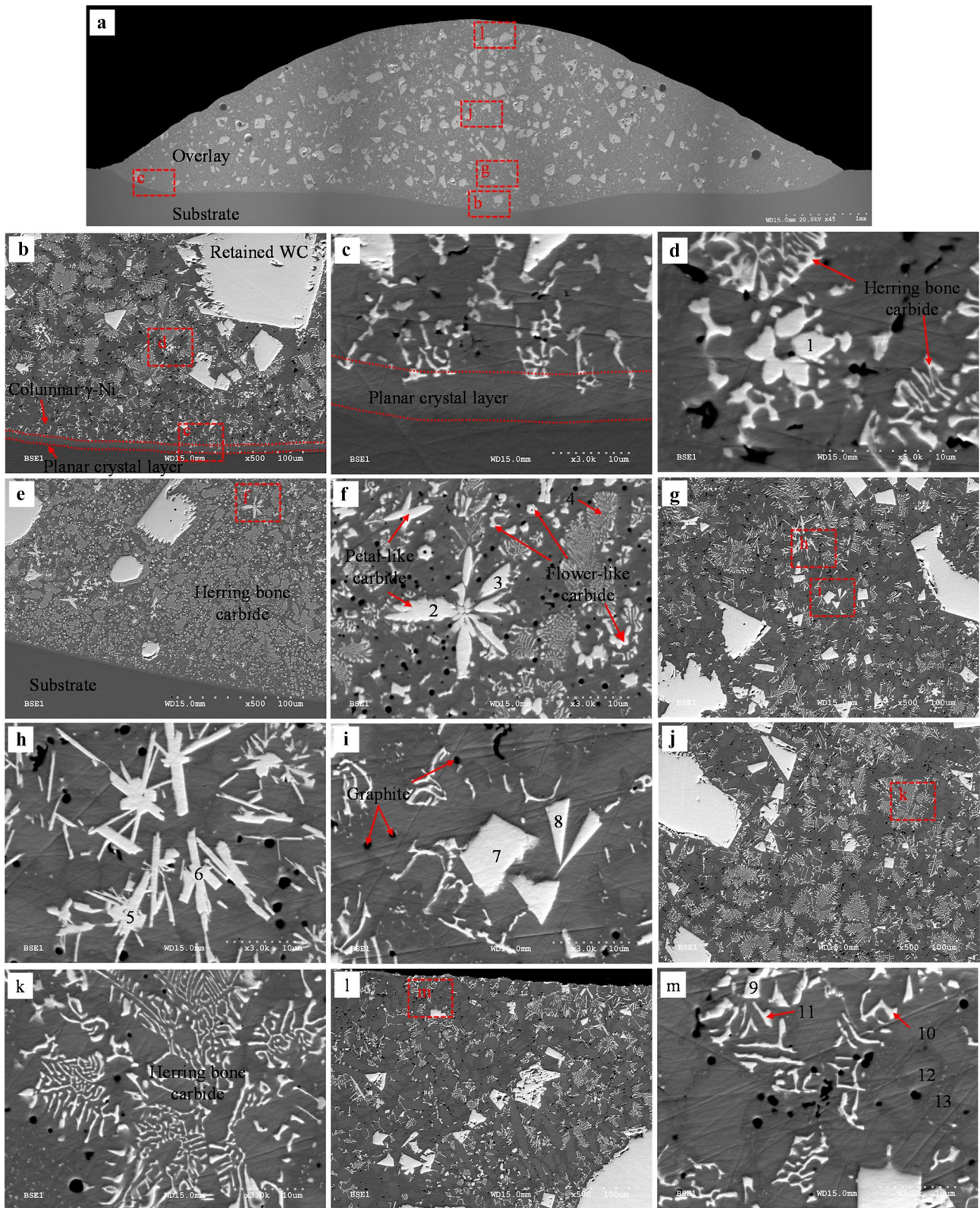


Fig. 19 BSE images of sample 16 (*AIP*: 2.95 kW): **a** overlay cross-section; **b** interface of the substrate/overlay; **c** and **d** higher magnification of the selected area in **b**; **e** left toe interface; **f** higher magnification of the selected area in **e**; **g** lower region; **h** and **i** higher

magnification of the selected area in **g**; **j** middle region; **k** higher magnification of the selected area in **j**; **l** upper region; **m** higher magnification of the selected area in **l**

Table 10 EDS spot results of marked locations in Fig. 13

Elements (wt.%)	Point													
	1	2	3	4	5	6	7	8	9	10	11	12	13	14
C	7.48	6.10	19.84	20.48	18.67	20.79	51.15	14.71	19.47	20.62	19.78	19.31	4.44	4.58
O	0.00	0.00	0.11	0.23	0.11	0.00	0.00	0.37	0.00	0.00	0.01	0.13	0.00	0.00
Si	0.00	0.00	0.00	0.00	0.00	0.00	0.02	0.00	0.00	0.00	0.00	0.00	0.00	0.59
Cr	0.99	0.56	1.49	1.63	1.48	0.99	0.56	1.33	1.75	3.66	0.09	1.27	0.98	2.23
Fe	4.92	5.31	0.28	0.37	0.54	0.35	3.57	0.28	0.41	0.3	0.17	0.19	1.39	1.30
Ni	73.94	73.02	6.40	7.75	13.5	8.73	42.00	4.3	9.54	15.4	3.2	5.67	75.53	77.49
W	12.67	15.01	71.88	69.54	65.7	69.14	2.71	79.00	68.83	60.03	76.75	73.42	17.66	13.81

Table 11 EDS point results of marked locations in Fig. 15

Elements (wt.%)	Point										
	1	2	3	4	5	6	7	8	9	10	11
C	4.31	5.87	15.68	17.00	13.65	11.75	16.45	16.41	15.91	3.57	3.99
O	0.18	0.00	0.00	0.00	0.36	0.02	0.00	0.00	0.00	0.00	0.00
Si	0.01	0.30	0.00	0.00	0.00	0.00	0.00	0.00	0.00	0.16	0.36
Cr	0.83	1.93	1.99	0.93	2.05	3.83	3.14	4.00	3.52	0.98	1.48
Fe	13.60	11.57	3.80	2.52	2.67	3.81	2.70	2.18	2.22	9.00	7.92
Ni	65.98	61.29	15.88	11.58	7.58	12.19	16.69	13.56	14.96	72.25	74.19
W	15.09	19.03	62.66	67.98	73.68	68.4	61.02	63.85	63.39	14.05	12.06

Table 12 EDS point results of the marked locations in Fig. 17

Elements (wt.%)	Point													
	1	2	3	4	5	6	7	8	9	10	11	12	13	14
C	10.17	6.35	3.78	15.12	16.16	16.74	17.71	15.89	18.17	19.21	2.9	3.11	16.5	16.29
O	0.17	0.03	0.44	0.00	0.00	0.00	0.00	0.00	0.00	0.00	0.18	0.00	0.20	0.45
Si	0.00	0.17	0.15	0.00	0.00	0.00	0.00	0.25	0.00	0.00	0.31	0.45	0.00	0.00
Cr	0.83	1.02	0.66	1.06	0.90	1.23	1.39	1.41	3.46	3.92	0.87	1.19	3.32	3.24
Fe	21.46	23.3	24.60	7.78	8.07	8.87	7.98	9.56	3.67	2.78	16.16	13.55	2.96	2.80
Ni	49.88	62.45	61.50	47.3	47.59	36.14	29.56	45.74	13.34	7.01	67.34	73.51	10.55	7.69
W	17.48	6.67	8.87	28.74	27.27	37.02	43.36	27.15	61.36	67.08	12.24	8.19	66.47	69.52

Table 13 EDS point results of marked locations in Fig. 19

Elements (wt.%)	Point												
	1	2	3	4	5	6	7	8	9	10	11	12	13
C	16.61	13.92	13.82	7.63	15.73	15.32	19.88	18.41	15.35	16.46	15.86	5.58	6.68
O	0.00	0.41	0.27	0.15	0	0.02	0.37	0.29	0.74	0.17	0.07	0.26	0.04
Si	0.00	0.00	0.00	0.00	0.00	0.00	0.00	0.00	0.00	0.00	0.00	0.03	0.53
Cr	1.10	1.38	1.45	0.95	1.11	0.87	0.85	1.22	1.26	1.39	1.13	0.68	1.14
Fe	5.67	4.51	4.19	17.86	6.57	4.87	1.55	1.60	1.79	8.16	11.06	22.54	22.31
Ni	12.49	7.88	7.08	41.35	15.36	11.88	2.79	2.58	2.94	17.44	25.39	58.53	58.86
W	64.13	71.91	73.19	32.07	61.22	67.04	74.56	75.89	77.92	56.38	46.49	12.38	10.44

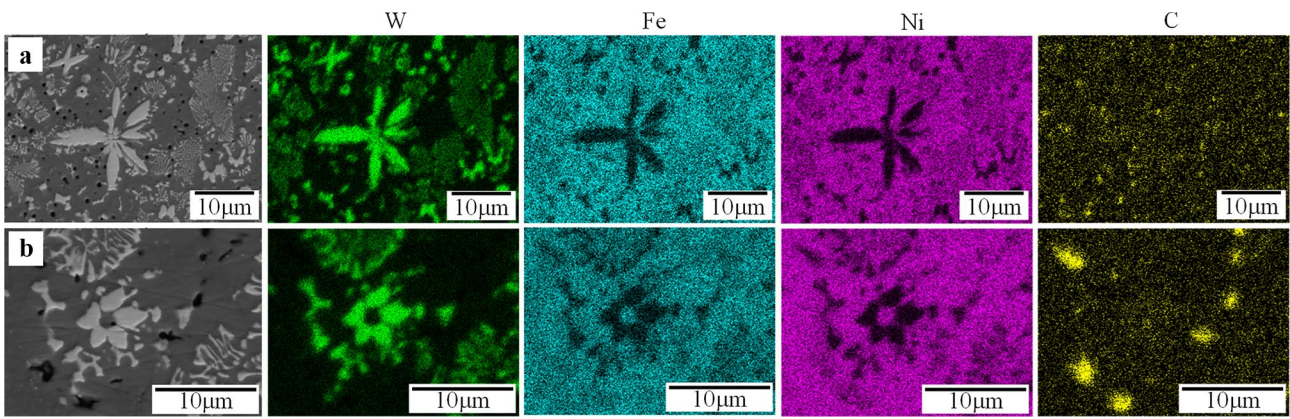


Fig. 20 EDS map of secondary carbide of sample 16 (*AIP*: 2.95 kW) from selected area

Fig. 21 Main effects plots of S/N ratio for **a** f_{WC} ; **b** η ; **c** *DL*; **d** *P*; **e** *DR*; **f** *W/H* (with dash lines indicating means of the S/N ratios)

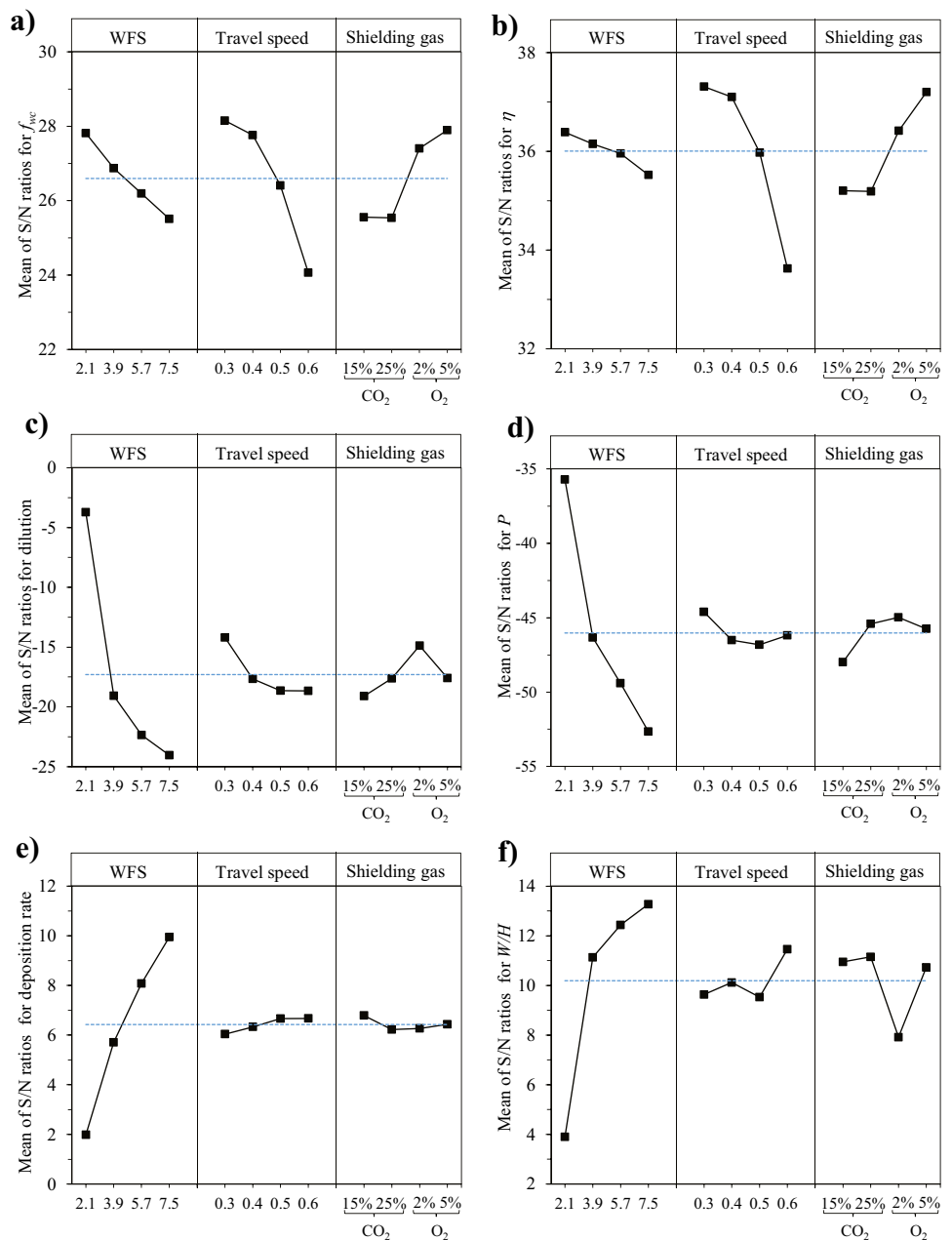


Table 14 S/N ratio results of the experiments

ID	WFS [m/min]	TS [m/min]	SG [%]	S/N ratio [dBi]						
				f_{WC}	η	DL	P	DR	W/H	
1	2.1	0.3	25% CO ₂	28.37	36.86	2.63	-31.39	1.55	4.94	
2	2.1	0.4	15% CO ₂	28.06	36.65	-4.95	-36.98	2.19	4.40	
3	2.1	0.5	2% O ₂	26.90	35.49	-5.87	-39.01	2.09	-0.63	
4	2.1	0.6	5% O ₂	27.92	36.54	-6.74	-35.49	2.10	6.89	
5	3.9	0.3	15% CO ₂	27.48	36.83	-19.91	-48.64	5.44	10.81	
6	3.9	0.4	25% CO ₂	26.69	36.31	-22.20	-47.92	5.53	12.15	
7	3.9	0.5	5% O ₂	27.87	36.98	-17.62	-43.83	6.05	11.12	
8	3.9	0.6	2% O ₂	25.45	34.47	-16.52	-44.98	5.78	10.48	
9	5.7	0.3	2% O ₂	28.99	38.02	-16.49	-45.68	7.56	10.54	
10	5.7	0.4	5% O ₂	28.01	37.75	-22.91	-50.94	7.96	12.63	
11	5.7	0.5	25% CO ₂	25.99	36.08	-24.76	-49.56	7.89	12.81	
12	5.7	0.6	15% CO ₂	21.79	31.98	-25.24	-51.47	8.88	13.77	
13	7.5	0.3	5% O ₂	27.77	37.54	-23.07	-52.75	9.61	12.27	
14	7.5	0.4	2% O ₂	28.29	37.69	-20.61	-50.20	9.63	11.29	
15	7.5	0.5	15% CO ₂	24.87	35.34	-26.35	-54.86	10.62	14.83	
16	7.5	0.6	25% CO ₂	21.10	31.51	-26.16	-52.82	9.91	14.72	

Table 15 Taguchi's recommended processing parameters for overlay quality improvement

Quality criterion	Recommended process control parameter				Remark
	WFS [m/min]	TS [m/min]	SG [%]	Predicted S/N [dBi]	
f_{WC}	2.1	0.3	5% O ₂	30.66	The recommended parameters are disadvantageous for deposition rate and W/H Disadvantageous for f_{WC} , η , DL, and P
η	2.1	0.3	5% O ₂	38.89	
DL	2.1	0.3	2% O ₂	1.78	
P	2.1	0.3	2% O ₂	-33.24	
DR	7.5	0.6	15% CO ₂	10.24	
W/H	7.5	0.6	25% CO ₂	15.58	

Table 16 Selected confirmation tests to improve overlay quality by prioritizing f_{WC} and η

Confirmation test	WFS [m/min]	TS [m/min]	SG [%]	S/N ratio of f_{WC}			S/N ratio of η		
				Predicted [dBi]	Experimental [dBi]	Error [%]	Predicted [dBi]	Experimental [dBi]	Error [%]
V1	2.1	0.3	5% O ₂	30.66	27.07	6.78	38.89	35.59	4.82
V2	3.9	0.3	5% O ₂	29.73	28.71	3.43	38.66	37.77	2.30

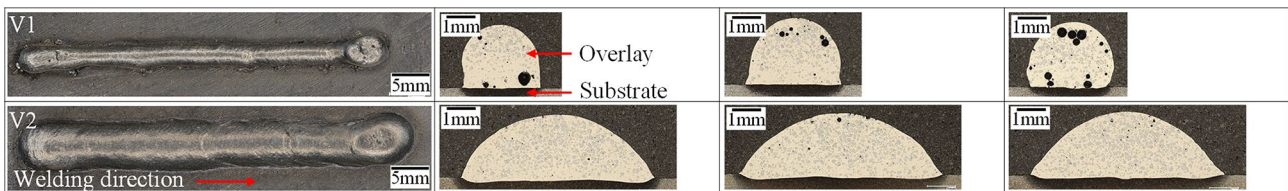


Fig. 22 Top and cross-sectional views of confirmation test samples

3.4 Recommended processing parameters for overlay quality improvement

Figure 21 and Table 14 show the main effect plots of the S/N ratio for f_{WC} , η , DL , P , DR , and W/H , in accordance with the respective goal of the experiments (see Table 6). In general, higher S/N ratio values suggest processing parameters that reduce the impact of noise components and variability and improve performance [61].

Table 15 lists the “best” parameters, independently selected based on S/N ratio and experiment goal for each quality criterion without considering interaction with other criteria. It can be seen that the recommended processing parameters to improve f_{WC} , η , DL , and P are opposite to what is required for improving DR and W/H . Therefore, it is difficult to find optimum processing parameters to meet all quality requirements; trade-offs are needed in engineering practices based on specific needs.

In weld cladding of Ni-WC MMC to steel substrates, keeping the DL below 10% is recommended to ensure a high-quality overlay [62]. Abioye et al. [63] proposed DL between 5 and 13% with θ less than 80° for Ni-WC MMC. As indicated by Choi et al. [4], DL below 1% is inadequate for oil-sand applications, particularly those involving mechanical impact loading. Moreover, Zhao et al. [44] suggested a DL of at least 1% for a satisfactory metallurgical bond between the substrate and the overlay. Hence, considering our targeted applications, it is rational to aim the DL of 1–10%. At this DL range (1–10%), the average f_{WC} in our experiments varied between 19 and 28%, as shown in Fig. 12. Furthermore, W/H greater than two is recommended for weld cladding to avoid a lack of fusion in subsequent passes [50, 64, 65].

It is known that f_{WC} and η are the most significant quality factors for Ni-WC MMC overlays compared to other criteria. On that basis, it seems that WFS at 2.1 m/min should be the best choice; however, weld cladding with WFS at 2.1 m/min could result in W/H smaller than two, as is the case for experiment runs 1–3 (see Fig. 9 and Table 9). The next in line is WFS of 3.9 m/min, which will keep the DL under 10% and can significantly improve the DR and W/H , but does not cause a drastic reduction in f_{WC} and η (see Fig. 9). As to the SG mixture, the one with 5% O_2 addition seems to be the best choice to improve f_{WC} and η .

3.5 Confirmation tests

Based on the deliberations in Section 3.4 and in reference to Table 15, TS of 0.3 m/min, SG with 5% O_2 addition, and WFS of 2.1 and 3.9 m/min are selected for the two intended confirmation tests (as listed in Table 16). Figure 22 illustrates the top view and transverse cross-sectional images of the resultant weld bead tracks, showing excellent

Table 17 Confirmation test results

ID	WFS [m/min]	TS [m/min]	SG [%]	I_{avg} [A]	V_{avg} [V]	HI [kJ/mm]	AIP [kW]	f_{WC} [%]	η [%]	DL [%]	P [mm]	DR [kg/h]	W [mm]	H [mm]	W/H	θ [°]
V1	2.1	0.3	5% O ₂	60.15	9.14	0.16	0.79	27.06	71.34	1.01	52.67	1.15	2.91	2.27	1.29	96.33
V2	3.9	0.3	5% O ₂	88.33	9.67	0.26	1.28	27.29	77.46	7.10	184.00	1.87	6.91	2.18	3.17	56.83

metallurgical bonding to the substrate without crack. The values of f_{WC} , η , DL , and weld bead geometry (P , WH , and θ) are summarized in Table 17. It can be seen that there is a good agreement between predicted values and experimental data as far as S/N ratios for f_{WC} and η are concerned, with marginal errors varying from 2.30 to 6.78% (see Table 16).

The first confirmation test at WFS of 2.1 m/min yielded weld bead geometry that is not suitable for weld cladding (albeit with high f_{WC} and η and with low DL). In contrast, the second confirmation test at WFS of 3.9 m/min achieved not only the same high level of f_{WC} and η as the first test but with much-improved weld bead geometry and higher DR , achieving much-improved overlay quality. Both tests are designed based on Taguchi analysis, and the outcomes are fully in line with the Taguchi prediction; the desired/predicted improvement of overlay quality is realized through the Taguchi DOE method. In short, the present investigation is a strong testimony of the power and effectiveness of the Taguchi DOE method in process improvement for weld cladding of Ni-WC MMC overlays.

4 Conclusion

In this study, Ni-WC MMC overlays were deposited on an A36 steel substrate by employing the CMT process. Taguchi's design of experiments L16 was used to investigate the effects of CMT processing parameters (WFS , TS , and SG) on f_{WC} , η , DL , DR , and weld bead geometry. All experiments were successfully deposited with continuous and uniform bead profiles, and no visual defect was detected. The transverse cross-sections exhibit excellent metallurgical bonding to the substrate, an average porosity level of 1.42%, and uniform distribution of retained WC. The main conclusions can be drawn as follows:

1. No degradation seam is observed around the retained WC particles in the deposited samples due to the high dissolution resistance of mono-crystalline WC particles. However, there is inevitably partial dissolution of retained WC particles in the molten pool during deposition, promoting the formation of primary WC and secondary carbides in the matrix;
2. The overall overlay microstructures consist of retained WC fairly uniformly distributed within the matrix of γ -Ni and eutectic Ni/Ni₃B. The formation of primary WC can be seen in all of the samples. Secondary carbides are also observed, possibly in the form of W₂C and/or W-rich carbides for samples with low DL (i.e., AIP around 1.9 kW) and in the form of M₆C (Ni₂W₄C/Fe₃W₃C) for those with higher DL (i.e., $AIP > 2$ kW), respectively. In general, f_{WC} is reduced with increased

DL , where Fe from the substrate is more easily mixed into the overlay, leading to the excessive dissolution of WC;

3. Dilution is affected by several processing parameters. HI and arc impingement have opposing effects on penetration and thus DL and should be considered jointly. Higher DL ($> 15\%$) is associated with higher WFS (5.7–7.5 m/min) and higher TS (0.6 m/min), while lower DL (1–10%) is observed at lower WFS and lower TS ;
4. f_{WC} does not solely depend on HI or AIP , in contrast to the observations for standard GMAW processes as reported in the open literature. The most influential factor affecting f_{WC} is TS , followed by WFS . High f_{WC} (and η), together with a high DR and improved weld bead appearance, are achievable with the CMT process even at high HI ;
5. Weld bead characteristics and DR are mainly affected by WFS . TS has a notable effect on weld bead characteristics but has only a marginal effect on DR . HI and AIP are positively correlated with WH and DR ;
6. Improvements in η are achieved by using SG mixtures with O₂ additions. This may be due to an increase in the oxidation rate of nickel in the weld pool, improving the arc stability during the droplet formation period, which can eventually lead to an increase in f_{WC} . In addition, using O₂ addition results in a decrease in DL and WH , which remain almost unchanged when using CO₂. There is no obvious correlation between DR and the composition of SG mixtures;
7. In general, the processing parameters beneficial to f_{WC} , η , DL , and P will have a negative effect on DR and WH . Therefore, it is difficult to find a single set of optimized processing parameters to meet all quality requirements; trade-offs are needed in the engineering practices based on the needs for specific outcomes;
8. Two confirmation tests designed based on Taguchi analysis achieved the expected outcomes; the present investigation clearly demonstrates that the Taguchi DOE method is a powerful tool in process improvement for weld cladding of Ni-WC MMC overlays.

Acknowledgements This work is funded by the CWB Welding Foundation, the National Research Council of Canada (NRC), and the Natural Sciences and Engineering Research Council of Canada (NSERC). The authors are grateful to NRC-Vancouver for providing the required materials, facilities, and technical supports for the experimental work.

Funding Open Access provided by National Research Council Canada.

Data availability Not applicable.

Code availability Not applicable.

Declarations

Ethics approval Not applicable.

Consent to participate Not applicable.

Consent for publication Not applicable.

Conflict of interest The authors declare no competing interests.

Open Access This article is licensed under a Creative Commons Attribution 4.0 International License, which permits use, sharing, adaptation, distribution and reproduction in any medium or format, as long as you give appropriate credit to the original author(s) and the source, provide a link to the Creative Commons licence, and indicate if changes were made. The images or other third party material in this article are included in the article's Creative Commons licence, unless indicated otherwise in a credit line to the material. If material is not included in the article's Creative Commons licence and your intended use is not permitted by statutory regulation or exceeds the permitted use, you will need to obtain permission directly from the copyright holder. To view a copy of this licence, visit <http://creativecommons.org/licenses/by/4.0/>.

References

- Wang S-H, Tadic D, Jiang J, Mckinnell J (2016) Weld cladding for mining and mineral processing: a Canadian perspective. *CWA J* 16:52–66
- National Research Council of Canada, Associate Committee on Tribology (1986) A strategy for tribology in Canada: enhancing reliability and efficiency through the reduction of wear and friction. <https://doi.org/10.4224/21272321>
- Anderson M, Chiovelli S, Hoskins S (2004) Improving reliability and productivity at Syncrude Canada Ltd. through materials research: past, present, and future. *CIM Bull* 97:1–6
- Choi L, Wolfe T, Yarmuch M, Gerlich A (2010) Effect of welding parameters on tungsten carbide - metal matrix composites produced by GMAW effect of welding parameters on tungsten carbide - metal matrix composites produced by GMAW. *Can Weld Assoc Conf*
- Mendez PF, Barnes N, Bell K et al (2014) Welding processes for wear resistant overlays. *J Manuf Process* 16:4–25. <https://doi.org/10.1016/j.jmapro.2013.06.011>
- Fisher G, Wolfe T, Meszaros K (2013) The effects of carbide characteristics on the performance of tungsten carbide-based composite overlays, deposited by plasma-transferred arc welding. *J Therm Spray Technol* 22:764–771. <https://doi.org/10.1007/s11666-012-9877-4>
- Flores JF, Neville A, Kapur N, Gnanavelu A (2009) An experimental study of the erosion-corrosion behavior of plasma transferred arc MMCs. *Wear* 267:213–222. <https://doi.org/10.1016/j.wear.2008.11.015>
- Chakraborty G, Kumar N, Das CR et al (2014) Study on microstructure and wear properties of different nickel base hardfacing alloys deposited on austenitic stainless steel. *Surf Coatings Technol* 244:180–188. <https://doi.org/10.1016/j.surfcoat.2014.02.013>
- Liyanage T, Fisher G, Gerlich AP (2012) Microstructures and abrasive wear performance of PTAW deposited Ni-WC overlays using different Ni-alloy chemistries. *Wear* 274–275:345–354. <https://doi.org/10.1016/j.wear.2011.10.001>
- Liyanage T (2010) Microstructure and properties of Ni-alloy and Ni-WC composite overlays. 1–108. <https://doi.org/10.7939/R3HB0Z>
- Segar R (2013) Effect of tungsten carbides properties of overlay welded WC/NiSiB composite coatings. 64
- Ortiz A, García A, Cadenas M et al (2017) WC particles distribution model in the cross-section of laser cladded NiCrBSi + WC coatings, for different wt% WC. *Surf Coatings Technol* 324:298–306. <https://doi.org/10.1016/j.surfcoat.2017.05.086>
- Sundaramoorthy R, Tong SX, Parekh D, Subramanian C (2017) Effect of matrix chemistry and WC types on the performance of Ni-WC based MMC overlays deposited by plasma transferred arc (PTA) welding. *Wear* 376–377:1720–1727. <https://doi.org/10.1016/j.wear.2017.01.027>
- Liu A, Li D, Meng F, Sun H (2017) Metal-matrix composite fabricated with gas tungsten arc melt injection and precoated with NiCrBSi alloy to increase the volume fraction of WC particles. *Sci Eng Compos Mater* 24:195–202. <https://doi.org/10.1515/secm-2014-0221>
- Schreiber F, Allebrodt B, Erpel T (2019) Hardfacing material solutions for high performance coatings in wear and corrosion applications. *Adv Technol Mater* 43:21–25. <https://doi.org/10.24867/atm-2018-2-004>
- Zhao S, Xu S, Huang Y, Yang L (2021) Laser hot-wire cladding of Ni/WC composite coatings with a tubular cored wire. *J Mater Process Technol* 298:117273. <https://doi.org/10.1016/j.jmatprotec.2021.117273>
- Badisch E, Kirchgaßner M (2008) Influence of welding parameters on microstructure and wear behaviour of a typical NiCrBSi hardfacing alloy reinforced with tungsten carbide. *Surf Coatings Technol* 202:6016–6022. <https://doi.org/10.1016/j.surfcoat.2008.06.185>
- Vespa P, Pinard PT, Gauvin R, Brochu M (2012) Analysis of WC/Ni-based coatings deposited by controlled short-circuit MIG welding. *J Mater Eng Perform* 21:865–876. <https://doi.org/10.1007/s11665-011-9947-7>
- Günther K, Bergmann JP (2018) Understanding the dissolution mechanism of fused tungsten carbides in Ni-based alloys: an experimental approach. *Mater Lett* 213:253–256. <https://doi.org/10.1016/j.matlet.2017.11.088>
- Guest SD (2014) Depositing Ni-WC wear resistant overlays with hot-wire assist technology. Dissertation, University of Alberta
- Scott KM (2011) Heat transfer and calorimetry of tubular Ni / WC wires deposited with GMAW. Dissertation, University of Alberta
- Guest SD, Chapuis J, Wood G, Mendez PF (2014) Non-wetting behaviour of tungsten carbide powders in nickel weld pool: new loss mechanism in GMAW overlays. *Sci Technol Weld Join* 19:133–141. <https://doi.org/10.1179/1362171813Y.0000000178>
- Günther K, Liefeth J, Henckell P et al (2018) Influence of processing conditions on the degradation kinetics of fused tungsten carbides in hardfacing. *Int J Refract Met Hard Mater* 70:224–231. <https://doi.org/10.1016/j.ijrmhm.2017.10.015>
- Kim D, Rhee S, Park H (2002) Modelling and optimization of a GMA welding process by genetic algorithm and response surface methodology. *Int J Prod Res* 40:1699–1711. <https://doi.org/10.1002/qua.20773>
- Sathish T, Rangarajan S, Muthuram A, Kumar RP (2020) Analysis and modelling of dissimilar materials welding based on K-nearest neighbour predictor. *Mater Today Proc* 21:108–112. <https://doi.org/10.1016/j.matpr.2019.05.371>
- Imoudou NE, Ayele YZ, Barabadi A (2018) The characteristic of cold metal transfer (CMT) and its application for cladding. *IEEE Int Conf Ind Eng Eng Manag* 2017-Decem:1883–1887. <https://doi.org/10.1109/IEEM.2017.8290218>
- Cao R, Feng Z, Chen JH (2014) Microstructures and properties of titanium-copper lap welded joints by cold metal transfer technology. *Mater Des* 53:192–201. <https://doi.org/10.1016/j.matdes.2013.06.030>

28. Grzybicki M, Jakubowski J (2013) Comparative tests of steel car body sheet welds made using CMT and MIG/MAG methods. *Weld Int* 27:610–615. <https://doi.org/10.1080/09507116.2011.606147>
29. Gungor B, Kaluc E, Taban E, Aydin SIK (2014) Mechanical and microstructural properties of robotic cold metal transfer (CMT) welded 5083–H111 and 6082–T651 aluminum alloys. *Mater Des* 54:207–211. <https://doi.org/10.1016/j.matdes.2013.08.018>
30. Näkki J (2018) Properties of alloy 625 claddings made with laser and CMT methods. Dissertation, Tampere University of Technology
31. Pickin CG, Young K (2006) Evaluation of cold metal transfer (CMT) process for welding aluminium alloy. *Sci Technol Weld Join* 11:583–585. <https://doi.org/10.1179/174329306X120886>
32. Cao R, Yu G, Chen JH, Wang PC (2013) Cold metal transfer joining aluminum alloys-to-galvanized mild steel. *J Mater Process Technol* 213:1753–1763. <https://doi.org/10.1016/j.jmatprotec.2013.04.004>
33. Ola OT, Doern FE (2014) A study of cold metal transfer clads in nickel-base INCONEL 718 superalloy. *Mater Des* 57:51–59. <https://doi.org/10.1016/j.matdes.2013.12.060>
34. Astm A36/A36M-19 (2019) Standard specification for carbon structural steel. ASTM Int West Conshohocken, PA. https://doi.org/10.1520/A0036_A0036M-19
35. COR@FACE 164 MC datasheet. <http://www.cor-met.com/products/hardfacing>. Accessed 13 Apr 2022
36. Chen M, Zhang D, Wu C (2017) Current waveform effects on CMT welding of mild steel. *J Mater Process Technol* 243:395–404. <https://doi.org/10.1016/j.jmatprotec.2017.01.004>
37. Kumar N, Devarajan PK, Arungalai Vendan S, Shanmugam N (2017) Prediction of bead geometry in cold metal transfer welding using back propagation neural network. *Int J Adv Manuf Technol* 93:385–392. <https://doi.org/10.1007/s00170-016-9562-8>
38. Melfi T (2010) New code requirements for calculating heat input. *Weld J* 89
39. Joseph A, Harwig D, Farson DF, Richardson R (2003) Measurement and calculation of arc power and heat transfer efficiency in pulsed gas metal arc welding. *Sci Technol Weld Join* 8:400–406. <https://doi.org/10.1179/136217103225005642>
40. Pepe N, Egerland S, Colegrove PA et al (2011) Measuring the process efficiency of controlled gas metal arc welding processes. *Sci Technol Weld Join* 16:412–417. <https://doi.org/10.1179/1362171810Y.0000000029>
41. Arevalo HDH, Vilarinho LO (2012) Desenvolvimento e avaliação de calorímetros por nitrogênio líquido e fluxo contínuo para medição de aporte térmico. *Soldag Inspeção* 17:236–250. <https://doi.org/10.1590/S0104-92242012000300008>
42. Zhao S, Yang L, Huang Y, Xu S (2021) A novel method to fabricate Ni/WC composite coatings by laser wire deposition: processing characteristics, microstructural evolution and mechanical properties under different wire transfer modes. *Addit Manuf* 38:101738. <https://doi.org/10.1016/j.addma.2020.101738>
43. Taguchi G, Yokoyama Y (1993) Taguchi methods: design of experiments. American Supplier Institute
44. Zhao S, Yang L, Huang Y, Xu S (2020) Feasibility study of producing Ni/WC composite coatings by laser deposition with a tubular cored wire. *J Mater Process Technol* 285. <https://doi.org/10.1016/j.jmatprotec.2020.116745>
45. Liu W, Gao D (2021) International Journal of Refractory Metals and Hard Materials Microstructure and wear of Ni-WC hardfacing used for steel-body PDC bits. *Int J Refract Met Hard Mater* 101:105683. <https://doi.org/10.1016/j.ijrmhm.2021.105683>
46. Günther K, Bergmann JP (2021) Experimental approach to determine the impact of the droplet transfer mode on the degradation of fused tungsten carbides during GMAW. *Int J Refract Met Hard Mater* 101:105692. <https://doi.org/10.1016/j.ijrmhm.2021.105692>
47. Wong Y-R, Ling S-F (2014) An investigation of dynamical metal transfer in GMAW—effects of argon shielding gas. *J Mater Process Technol* 214:106–111. <https://doi.org/10.1016/j.jmatprotec.2013.08.003>
48. Bitharas I, McPherson NA, McGhie W et al (2018) Visualisation and optimisation of shielding gas coverage during gas metal arc welding. *J Mater Process Technol* 255:451–462. <https://doi.org/10.1016/j.jmatprotec.2017.11.048>
49. Wang LL, Lu FG, Wang HP et al (2014) Effects of shielding gas composition on arc profile and molten pool dynamics in gas metal arc welding of steels. *J Phys D Appl Phys* 47. <https://doi.org/10.1088/0022-3727/47/46/465202>
50. Silva CC (2013) Weld overlay bt - encyclopedia of tribology. In: Wang QJ, Chung Y-W (eds) Springer. US, Boston, MA, pp 4094–4101
51. Liyanage T, Fisher G, Gerlich AP (2010) Influence of alloy chemistry on microstructure and properties in NiCrBSi overlay coatings deposited by plasma transferred arc welding (PTAW). *Surf Coatings Technol* 205:759–765. <https://doi.org/10.1016/j.surfcoat.2010.07.095>
52. Mezrag B, Deschaux-Beaume F, Benachour M (2015) Control of mass and heat transfer for steel/ aluminium joining using cold metal transfer process. *Sci Technol Weld Join* 20:189–198. <https://doi.org/10.1179/1362171814Y.0000000271>
53. Kou S (2002) Welding metallurgy. John Wiley & Sons Inc, Hoboken, NJ, USA
54. Dupont JN (2011) Fundamentals of weld solidification. In: Welding fundamentals and processes. ASM International, pp 96–114
55. Zhao S, Yang L, Huang Y, Xu S (2020) Enrichment of in-situ synthesized WC by partial dissolution of ex-situ eutectoid-structured WC/W2C particle in the coatings produced by laser hot-wire deposition. *Mater Lett* 281:128641. <https://doi.org/10.1016/j.matlet.2020.128641>
56. Gu D, Jia Q (2014) Novel crystal growth of in situ WC in selective laser-melted W - C - Ni ternary system. *J Am Ceram Soc* 97:684–687. <https://doi.org/10.1111/jace.12828>
57. Shu D, Li Z, Zhang K et al (2017) In situ synthesized high volume fraction WC reinforced Ni-based coating by laser cladding. *Mater Lett* 195:178–181. <https://doi.org/10.1016/j.matlet.2017.02.076>
58. Li Y, Dong S, Yan S et al (2018) Surface remanufacturing of ductile cast iron by laser cladding Ni-Cu alloy coatings. *Surf Coatings Technol* 347:20–28. <https://doi.org/10.1016/j.surfcoat.2018.04.065>
59. Singleton MF, Nash P (1991) Phase diagrams of binary nickel alloys. *ASM Int* 50–55
60. Zhao S, Zhao S, Jia C et al (2022) Insights into microstructural evolution and dissolution characteristics of reinforced particles in tungsten carbide-nickel composite coatings prepared by laser hot-wire deposition. *Int J Refract Met Hard Mater* 103:105720. <https://doi.org/10.1016/j.ijrmhm.2021.105720>
61. Rojas JGM, Ghasri-Khouzani M, Wolfe T et al (2021) Preliminary geometrical and microstructural characterization of WC-reinforced NiCrBSi matrix composites fabricated by plasma transferred arc additive manufacturing through Taguchi-based experimentation. *Int J Adv Manuf Technol* 113:1451–1468. <https://doi.org/10.1007/s00170-020-06388-2>
62. Davis JR (1993) Hardfacing, weld cladding, and dissimilar metal joining. In: ASM Handbook, Volume 06 - Welding, Brazing, and Soldering. ASM International
63. Abioye TE, Folkes J, Clare AT (2013) A parametric study of Inconel 625 wire laser deposition. *J Mater Process Technol* 213:2145–2151. <https://doi.org/10.1016/j.jmatprotec.2013.06.007>
64. Rajeev GP, Kamaraj M, Bakshi SR (2014) Al-Si-Mn alloy coating on aluminum substrate using cold metal transfer (CMT) welding technique. *Jom* 66:1061–1067. <https://doi.org/10.1007/s11837-014-0970-7>

65. Ribeiro RA, dos Santos EBF, Assunção PDC et al (2015) Predicting weld bead geometry in the novel CW-GMAW Process. *Weld J* 94:301s–311s

Publisher's Note Springer Nature remains neutral with regard to jurisdictional claims in published maps and institutional affiliations.